NANOSTRUCTURED PARTICULATE AND FIBROUS MATERIALS FOR FUEL CELL ELECTRODE APPLICATION

(粒子状及び繊維状ナノ構造材料の合成と燃料電池電極への応用)

By

SUMIHITO SAGO

HIROSHIMA UNIVERSITY

MARCH 2015

NANOSTRUCTURED PARTICULATE AND FIBROUS MATERIALS FOR FUEL CELL ELECTRODE APPLICATION

(粒子状及び繊維状ナノ構造材料の合成と燃料電池電極への応用)

A Thesis submitted to
The Department of Chemical Engineering
Graduate School of Engineering
Hiroshima University

By

SUMIHITO SAGO

In Partial Fulfillment of the Requirements
For the Degree of
Doctor of Engineering

Hiroshima University
March 2015

Approved by

Professor Kikuo Okuyama
Advisor

Abstract

The objective of this thesis is to systematically investigate the synthesis of nanostructured particle and fibrous materials using spray process (i.e. spray pyrolysis and electrospray) and their application. Various types of nanostructured particles such as dense, hollow and porous particles and nanofiber have been developed and their application as catalyst was examined subsequently. The structural properties and electrocatalytic activity of the prepared nanostructured catalyst materials are reported thoroughly.

Chapter 1 describes the background, previous research, objectives and outline of thesis.

Chapter 2 describes the synthesis and evaluation of porous carbon derived from phenolic resin using a fast and facile spray pyrolysis method has been studied for use as a new electrocatalyst support material. By adding polystyrene latex nanoparticles as a template to the phenolic resin precursor, self-organized macroporous carbon structure was first developed. The mass ratio of phenolic resin to PSL at 0.625 gave the optimum porous morphology. Pt nanoparticles (~20 wt %) were grown on the carbon surface using a standard industrial impregnation method. Well-dispersed Pt nanoparticles of average size 3.91 nm were observed on the surface of porous carbon particles. The high catalytic performance of porous Pt/C electrocatalyst was confirmed by the high mass activity and electrochemically active surface area, which were 450.81 mA mg^{-1}-Pt and 81.78 m^2 g^{-1}-Pt, respectively. The porous Pt/C catalyst obtains two times higher mass activity than that of the commercial Pt/C catalyst and performs

excellent durability under acid conditions.

Chapter 3 describes that the synthesis of nanostructured carbon particle is challenging because of the poor ability of polymeric precursors to self-assemble during spray pyrolysis. Here, we report a facile method for designing self-organized nanostructured carbon particles. A dual polymer system of phenolic resin and electrically charged polystyrene latex is ultrasonically spray pyrolyzed to produce either hollow or porous carbon particles. The hollow and porous carbon particles exhibit high CO_2 adsorption capacities of 3.0 and 4.8 mmol g^{-1}, respectively.

Chapter 4 describes the synthesis of Pt/SnO_2 nanofibers via electrospinning. The unique electrochemical properties were in evidence based on the activity that allowed a hydrogen oxidation reaction and inhibit an oxygen reduction reaction. A high electrochemically active surface area value of 81.17 m^2/g-Pt was achieved with ultra-low Pt loading (4.03 wt.%). The kinetics of a hydrogen oxidation reaction was investigated using a linear sweep voltammetry technique under a hydrogen atmosphere. A diffusion-limited current was achieved at 0.07 V and was stable at a high potential. This preparation technique shows great promise for the design of anode electrocatalyst material for fuel cells.

Chapter 5 describes a facile method to synthesize Pt nanoparticles on the electrospun SnO_2 fiber matrix is presented. Precursors contained tin chloride pentahydrate, hexachloroplatinic acid, polyacrylonitrile, and *N,N*-dimethylformamide was electrospun subsequent calcination at 500 ^{o}C for 4 h. It is shown that Pt nanoparticles were grown on SnO_2 fiber matrix without any formation of PtO. Pt nanoparticles size was span in the range of 6-32 nm, by adjusting the concentration of

polyacrylonitrile. The electrochemically active surface area of Pt/SnO_2 fibers was found very competitive to the commercially available electrocatalyst. This work demonstrates that Pt/SnO_2 fibers can be generated by a facile electrospinning process.

The conclusion of this thesis is mentioned in **Chapter 6**.

Contents

Abstract ii

Contents .....

Chapter 1

Introduction 1

1.1. Background 1

1.2. Nanostructured Materials for Electronics Application 5

1.2.1. Synthesis of Nanostructured Particles 5

1.2.2. Synthesis of Nanostuctured Fibers 8

1.2.3. Nanostructured of catalyst Based Material 10

1.2.4. Catalyst for Low Temperature Fuel Cell-Basic Principle 11

1.3. Objectives and Outline of Thesis 14

1.4. References 17

Chapter 2

Self-Organized Macroporous Carbon Structure Derived from Phenolic Resin via Spray Pyrolysis for High-Performance Electrocatalyst 19

2.1. Introduction 19

2.2. Experiment 21

Preparation of Porous Pt/C Electrocatalyst 21

Characterizations 21

2.3. Results and discussion 23

2.4. Conclusions 37

2.5 References 38

Chapter 3

Aerosol synthesis of Self-Organized Nanostructured Hollow and Porous Carbon Particles using a Dual Polymer System 41

3.1. Introduction 41

3.2 Experimental 42

Characterizations 43

3.3. Results and discussions 43

3.4. Conclusions and outlook 56

3.5. References 58

Chapter 4

Electrospun Pt/SnO_2 Nanofibers as an Excellent Electrocatalyst for Hydrogen Oxidation Reaction with ORR-blocking Characteristic 60

4.1. Introduction 60

4.2. Experiment 61

4.3. Results and discussion.....63

4.4. Conclusions 69

4.5. References 69

Chapter 5

In Situ Growth of Pt Nanoparticles on Electrospun SnO_2 Fibers for Anode Electrocatalyst Application 71

5.1. Introduction 71

5.2. Experiment 72

5.3. Results and discussions 74

5.4. Conclusions 80

5.5. References 82

6. Chapter 6
Conclusions 83

Appendix I: List of Figures .....

Appendix II: List of Tables .....

Chapter 1

Introduction

1.1. Background

Nanostructure materials are of great scientific interest because of their unique properties. They offer many advantages and remarkably properties compared with their macro scale counterparts, due to the size-dependent quantum effects that arise in the nanostructure materials [1-4]. They also offer solution in environmental issue arises by single nanoparticle, as shown in Figure 1.1 [5]. While the nanostructured materials are synthesized, the structure and morphology could be engineered to control their properties. Therefore, control over the shape of nanostructure materials is dispensable for their applications [6]. There are various types of nanostructure materials, such as nanoparticles, nanofiber, nanowire, nanotube, etc. Table 1.1 shows a list of nanostructured particles, and their potential applications [5]. One of nanostructured

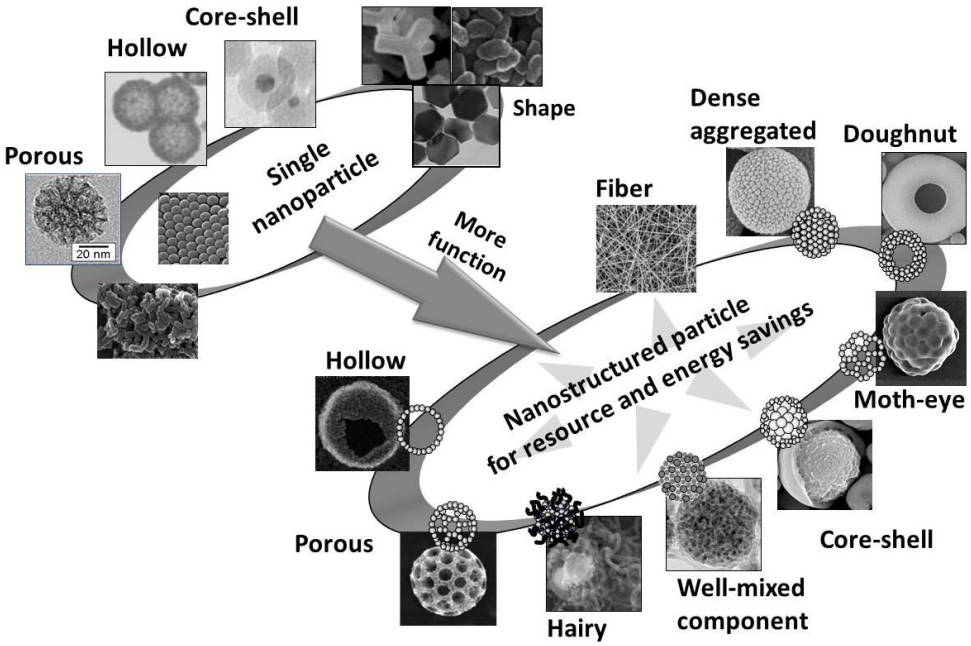

Fig. 1.1. Nanoparticle to fine structured particle for better functional applications.

Table 1.1. Features and applications of particles with various morphologies.

Nanostructured materials	Feature	Application
Aggregates particle	· high specific surface area · low temperature sintering	· catalyst carrier · electrode materials
Porous particle	· high specific surface area · low density/light · reducing raw materials	· catalyst · drug delivery · phosphor · insulator
Hollow particle	· low density/light · reducing raw materials · low refractive index	· antireflection materials · catalyst · drug delivery · phosphor · insulator
Doughnut particle	· specific optical property · high specific surface area · reducing raw materials	· catalyst · optical materials
Moth-eye hollow particle	· adjusting refractive index · low density/light · reducing raw materials	· catalyst · drug delivery · phosphor · optical materials
Core shell particle	· antiweatherability · reducing raw materials · adjusting refractive index	· catalyst · drug delivery · phosphor· optical materials
Composite particle (nanoparticle & nanoparticle)	· high specific surface area · hybrid functionality · immobilization of nanoparticle	· catalyst carrier · electrode materials · phosphor
Composite particle (nanoparticle & submicron particle)	· high specific surface area · immobilization of nanoparticle · reducing raw materials	· catalyst · phosphor
Composite particle (inorganic & organic)	· immobilization of nanoparticle · hybrid functionality	· optical materials · magnetic material · luminescence material · flame resisting material
Hairy particle	· high conductivity	· filler of nanocomposite materials

particles that I have been developed was Cerabine CZR PRESS (Figure 1.2). Its technology consists of the marriage of two time-proven technologies, oxide ceramics and pressable ceramics. This synergy combines the strength, fracture toughness and cementability of pure zirconia copings with the marginal integrity, versatility and beauty of pressable ceramics.

Fig. 1.2. Ceramic development for dental application.

Nanotube materials become a hot topic during these several decades due to its extraordinary thermal conductivity, mechanical and electrical properties. I have also developed carbon nanotube (CNT) during 1997-2003. CNTs are the strongest and stiffest materials yet discovered in terms of tensile strength and elastic modulus respectively, as shown in Figure 1.3. Techniques have been developed to produce nanotubes in sizeable quantities, including arc discharge, laser ablation, and chemical vapor deposition (CVD). Most of these processes take place in vacuum or with process gases. It means that high cost production and severe condition are necessary to produce nanotube. Thus, large scale production is still hindered.

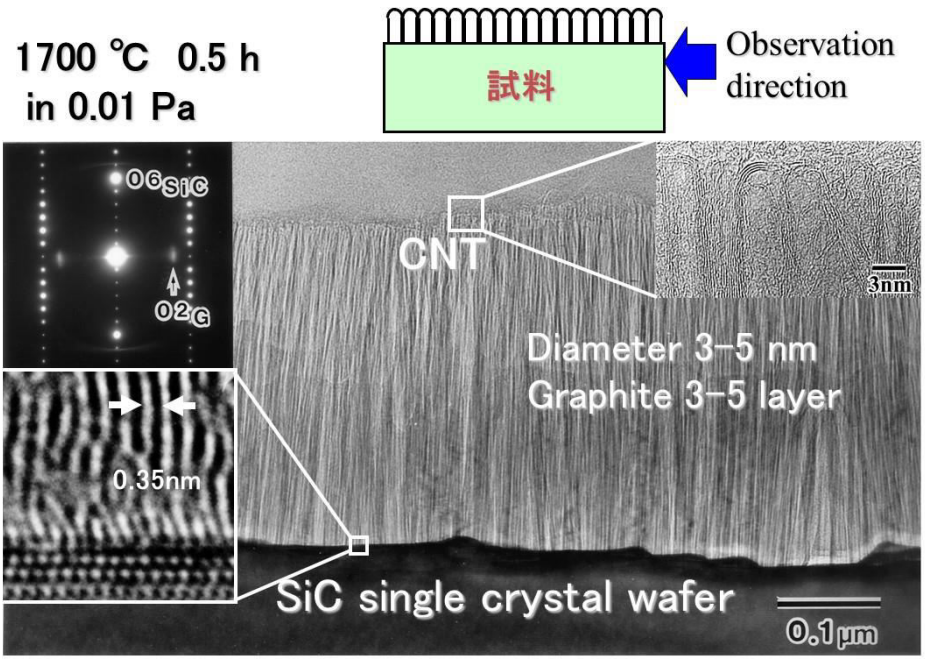

Fig. 1.3. TEM images of the prepared carbon nanotubes.

Nanowire and nanofiber materials are a one-dimensional (1D) nanostructure, with diameter in nanometer scale and length in hundreds micrometer scale for nanowire and millimeter up to centimeter scale for nanofiber. Nanowire has high Young`s moduli which is enable to use it on enhancing composites mechanically. They also may be used as tribological additives to improve friction characteristics and reliability of electronic transducers and actuators. However, the state-of-the-art of nanowire's research is still in a laboratory scale. The limited length of nanowire obtaining small surface area, while ultra-long nanofibers give more advantages such as large surface area per unit mass and flexibility in surface functionalities, and superior mechanical performance compared with any other known form of the materials. These outstanding properties make the nanofibers materials to be optimal candidates for many important applications [7].

The high demand of electronics device-based green energy have encourage thousands researcher to develop high performance material supporter for this type of

device. Combining my research background and my position as a company researcher, it is a challenge for me to develop novel methods to produce the functional nanostructured particles and fibers is critical to obtain high performance materials to be applied as a catalyst of fuel cell.

1.2. Nanostructured Materials for Electronics Application

1.2.1. Synthesis of Nanostructured Particles

Recently, there has been a significant effort to produce high-quality nanoparticles. There are several methods of synthesis of nanoparticles, which can be classified into two process types, which are "Top-down process" and "Bottom-up process". The principle of top-down process is break down the agglomerated particles to reduce the size. Bulk material will be mechanically grinding or comminuting to form particles either submicron or nanosized particles. On the other hand, the bottom-up process started from atomic or molecular level, agglomerated or growth via gas, solid or liquid phase synthesis to obtain nanoparticles.

Physical vapor deposition (PVD) and chemical vapor deposition (CVD) are some examples of gas-phase synthesis [8]. The primary advantages of the gas-to-particle conversion method are the small particle size (a few nanometers to micron), narrow size distribution and high purity of the product particles. However, as disadvantages, the formation of hard agglomerates in the gas phase leads to difficulties in preparing high-quality bulk materials. It is also difficult to synthesize multi-component materials, because of the differences in chemical reaction rate, vapor pressure, nucleation and growth rate which occur during the gas-to-particle conversion,

that may lead to non-uniform composition.

Solid-phase synthesis is unpopular method, due to the requirement of a very high temperature and long heating process to react several nanoparticles and formed the desired one. Otherwise, liquid-phase synthesis is the most popular of all. It can be classified into three different techniques: precipitation methods (e.g. co-precipitation, hydrolysis, redox-reaction, and sol-gel), special reaction field (e.g. hydrothermal supercritical fluid and microemulsion), and solvent evaporation methods (e.g. spray-pyrolysis and spray-drying).

All of the techniques that belong to liquid-phase method are relatively easy and simple method with reaction around room temperature. However, synthesis of particle using precipitation methods needs a long time process and carefully controlled condition. Special reaction field need high technology apparatus with necessity of special maintenance, which means high cost, is necessary and only small amount of product can be obtained from this technique. The above explanation shows that there will be a lot of difficulties to adjust the research using those techniques into large scale of industrial production. Thus, the most promising method for industrially application is solvent evaporation methods such as, spray-pyrolysis and spray-drying.

Spray-pyrolysis and spray-drying are specific types of droplet-to-particle aerosol methods which are simple and efficient to produce a variety of particles such as ceramic and organic particles ranging from nano- to micrometer sizes. In spray-pyrolysis, a liquid solution which contains the elements of the desired powder is atomized and introduced into a hot tubular reactor. In the reactor, the droplets dry and decompose to produce final particles. If the precursor solution does not decompose

during the process, the solution droplets simply dry to form the final particles. This method is called spray-drying. The final morphology of the product prepared using these both methods were influenced by the electrical and mechanical force occurred in the droplet as shown in Figure 1.4 [9]. Therefore, spray-pyrolysis is the most suitable method to design the morphology of nanoparticle prepared from organic source. Engineering of particles morphology becomes a crucial topic in the last decade. Since a specific morphology is required for a specific purpose. Selection of appropriate morphology is able to enhance the effectiveness of nanoparticle on the application. One of the popular applications of controlled morphology of nanoparticle is as catalyst based material.

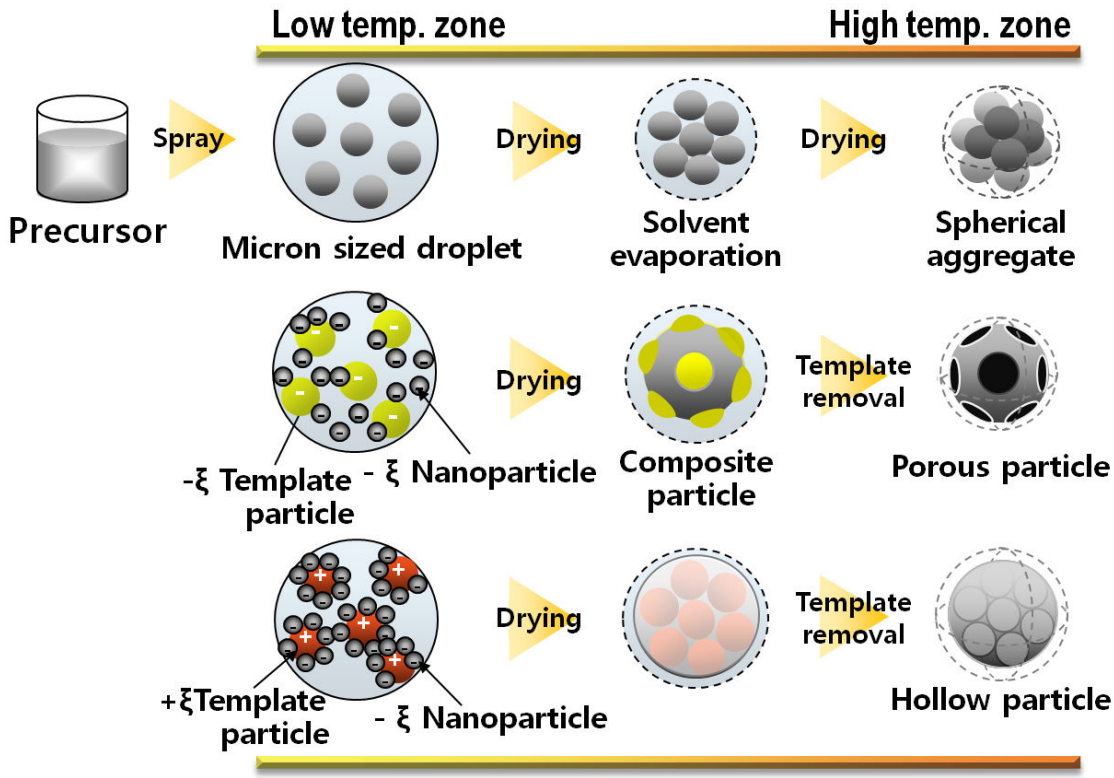

Fig. 1.4. A schematic illustration of particle formation on surface of charged colloidal particles.

1.2.2. Synthesis of Nanostructured Fibers

There are various method for preparing nanofibers materials such as drawing, template synthesis, phase separation, self-assembly, electrospinning, etc. In the drawing method, starting materials are dissolved in volatile solvent. The equipment apparatus consist of a pump and spinneret. There is an air outlet at the top of the tall shift and air in let at the bottom. The fiber spinining solution is forced under pressure from the storage tank to the spinning pump and then through the spinneret. When the fiber spinning solution emerging from spinneret meet the worm air, volatile solvent evaporates leaving the filaments, hence coagulation takes place and becomes dried before leaving the chamber. However, only a viscoelastic material that can undergo strong deformations while being cohesive enough to support the stresses developed during pulling can be made into nanofibers through drawing. The template method uses a membrane template (anodic aluminum oxide) to make nanofibers. This method is very useful to make nanometer fibrils from various raw materials such as polymer, metal, semiconductor, and carbon. However, template method cannot make one-by-one continuous nanofibers, and its length is very limited. Thus far, the electrospinning process seems to be the only method which can be further developed for mass production of one-by-one continuous nanofibers from various polymers [10].

The Electrospinning is a variant of the electrostatic spraying process (electrospray). Both of these techniques involve the use of a high voltage to induce the formation of a liquid jet. In electrospray, small droplets or particles are formed as a result of the varicose breakup of the electrified jet (composed of a highly viscous polymer solution) that is often present with a solution of low viscosity. In

electrospinning, a solid fiber is generated as the electrified jet (composed of a highly viscous polymer solution) is continuously stretched due to the electrostatic repulsions between the surface charges and the evaporation of solvent. Electrospray has found wide spread use in many areas including mass spectrometry, painting, inkjet printing, and manufacturing of particles with various size and compositions [10].

A schematic diagram to interpret electrospinning of polymer nanofibers is shown in Figure 1.5. There are basically three components to fulfill the process: a high voltage supplier, a capillary tube with a pipette or needle of small diameter, and a metal collecting screen. In the electrospinning process a high voltage is used to create an electrically charged jet of polymer solution or melt out of the pipette. Before reaching the collecting screen, the solution jet evaporates or solidifies, and is collected as an interconnected web of small fibers. One electrode is placed into the spinning solution/melt and the other attached to the collector. In most cases, the collector is simply grounded, as indicated in Figure 1.5. The electric field is subjected to the end of the capillary tube that contains the solution fluid held by its surface tension. This induces a charge on the surface of the liquid. Mutual charge repulsion and the contraction of the surface charges to the counter electrode cause a force directly opposite to the surface tension. As the intensity of the electric field is increased, the hemispherical surface of the fluid at the tip of the capillary tube elongates to form a conical shape known as the Taylor cone. Further increasing the electric field, a critical value is attained with which the repulsive electrostatic force overcomes the surface tension and the charged jet of the fluid is ejected from the tip of the Taylor cone. The discharged polymer solution jet undergoes an instability and elongation process, which

allows the jet to become very long and thin. Meanwhile, the solvent evaporates, leaving behind a charged polymer fiber. In the case of the melt the discharged jet solidifies when it travels in the air.

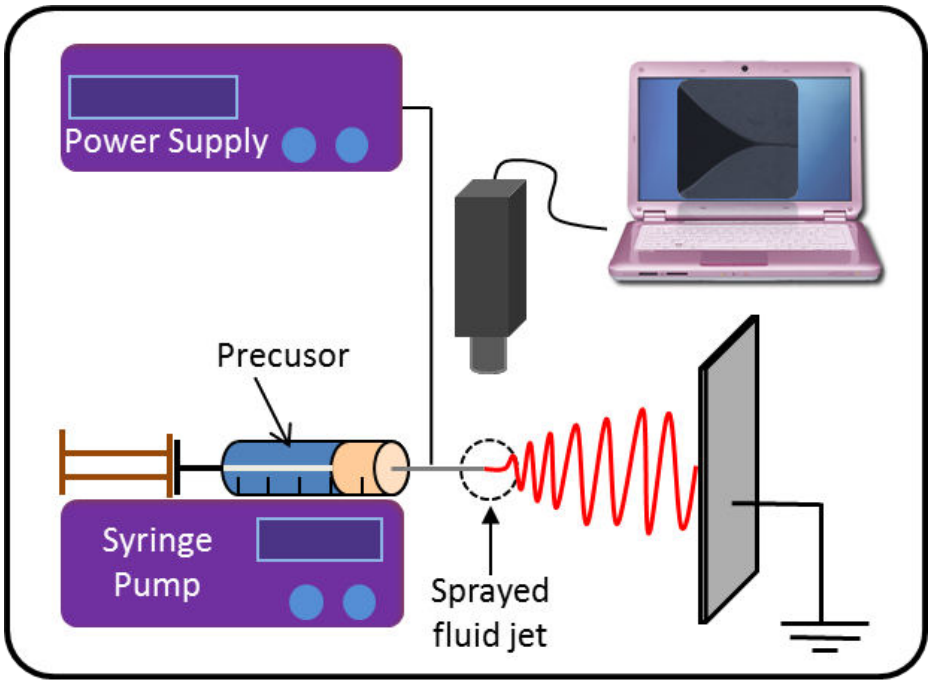

Fig. 1.5. Electrospining setup

1.2.3. Nanostructured of Catalyst Based Material

Catalyst becomes the hottest issue on the nanoparticle research in the last decade since its ability to provide an alternative reaction pathway to the reaction product. The rate of the reaction is increased as this alternative route has lower activation energy than the reaction route not mediated by the catalyst. The production of most industrially important chemicals involves catalysis. Research into catalysis is a major field in applied science and involves many areas of chemistry, notably in organometallic chemistry and materials science. Catalysis is relevant to many aspects of

environmental science, e.g. the catalytic converter in automobiles and the dynamics of the ozone hole. Catalytic reactions are preferred in environmentally friendly green chemistry due to the reduced amount of waste generated, as opposed to stoichiometric reactions in which all reactants are consumed and more side products are formed. Furthermore, in the case of future energy source, catalyst takes the main part of electrode, and contributes a very big effect to the efficiency of the electrode.

To date, development of catalyst still needs much attention. One way that will make a major breakthrough on the effectiveness surface area of the catalyst is by engineered its morphology. Creation of appropriate catalyst morphology is the key of the efficient fluid transport and increase the active surface area for catalytic reactions. The main studies in this thesis are development of catalysts for low temperature fuel cell (i.e. proton exchange membrane fuel cell PEMFC).

In the case of catalyst for PEMFC, high catalytic activity material such as carbon and SnO_2 are used to support the main catalyst of platinum (Pt), which was one of rare-earth and expensive materials. Appropriate morphology that support the three phase boundary (i.e. catalyst, gas phase, and electrolyte) is crucial to optimize the activity. Therefore, detail study on the morphological engineering of catalyst is very challenging.

1.2.4. Catalyst for Low Temperature Fuel Cell – Basic Principle

Alternative energy sources must be consider seriously to satisfy mankind`s ever-increasing energy needs which currently dominated by fossil fuels, petroleum and natural gas, which is increasing the environmental problems. Fuel cell is one of the

favorable future energy sources because of its ability to convert hydrogen into electricity in a highly efficient and environmentally manner.

Controlled morphology of carbon is attractive because it can be prepared relatively inexpensively from wide variety of low-cost precursors, it is typically biocompatible and quite chemically stable under non oxidizing condition, it has low density, high thermal conductivity, good electrical conductivity, mechanical stability and is easily to handle. Controlled morphology of carbon can be used as a catalyst support in proton exchange membrane fuel cell (PEMFC). Pt is widely used as an excellent catalyst for electrochemical reaction in PEMFC. However, its low-level abundance in nature creates a great barrier for the commercialization of PEMFC. Therefore, reducing the amount of Pt and increasing its active support becomes a big challenge. Catalyst support strongly influences the particle size and dispersion of Pt. A structure with high surface area is highly desirable for catalyst support, and the structural engineering of carbon nanoparticle into carbon microspheres which provide sufficient tunnel from one side of surface to another would allow good dispersion of Pt nanoparticles and rapid transport of reactant and product from the active catalyst sites to the bulk of fluid.

The electrochemical characterization of prepared catalyst for PEMFC application was performed using cyclic voltammetry (CV) and linear sweep voltammetry (LSV) measurement. It is necessary to make a good film of catalyst on the surface of working electrode for this measurement [11]. Catalyst electrochemical surface area in the working electrode is determined from CV measurement results and calculated using Equation 1.1:

$$ECSA(m^2 g_{Pt}^{-1}) = \left[\frac{Q_{H-adsorption}(C)}{210\mu C\, cm^{-2} L_{Pt}(mg_{Pt}\, cm^{-2}) Ag(cm^2)} \right] \quad (1.1)$$

where, ECSA is electrochemical surface area of catalyst reported in ($m^2 g_{Pt}^{-1}$); the charge of full coverage for clean polycrystalline Pt is Q_H = 210 μC cm^{-2} and is used as the conversion factor; L_{Pt} is the working electrode Pt loading (mg_{Pt} cm^{-2}) and A_g (cm^2) is the geometric surface area of the glassy carbon electrode (e.g. 0.196 cm^2 for glassy carbon with Ø = 5 mm).

Linier sweep voltammetry (LSV) measurement obtained oxygen reduction reaction (ORR) polarization curve which are measured at various rotation rate (i.e. 3600, 2500, 1600, 900, and 400 rpm) to obtain Koutecký-Levich plot. The electrocatalytic activity of catalyst is best compared by their mass- and area-specific activities using the mass-transport correction for thin-film rotating disk electrodes (RDEs, Equation 1.2):

$$I_k(A) = \frac{I_{\lim}(A) \times I(A)}{(I_{\lim} - I)} \quad (1.2)$$

where: I_k is the kinetic current (A), and I_{lim} is the measured limiting current (A). First, ORR polarization curves are corrected by subtracting background current measured under identical condition under N_2 atmosphere without rotation. Then, I is the value of the curve at E = 0.9 V versus RHE. The Pt mass activities are estimated via calculation of I_k and normalization to the Pt loading of the disk electrode. The Pt specific activities are estimated via the calculation of I_k and normalizing to the Pt electrochemical surface area using Equation 1.3:

$$I_s(\mu A\, cm_{Pt}^{-2}) = \frac{I_k(A)}{\left(Q_{H-adsorption}(C) / 210\mu C\, cm_{Pt}^{-2}\right)} \quad (1.3)$$

1.3. Objectives and Outline of Thesis

Figure 1.6. shows the outline of this thesis. Here, synthesis and application of nanostructured materials as catalyst were investigated thoroughly. Various types of nanostructured materials have been synthesized and their properties were examined.

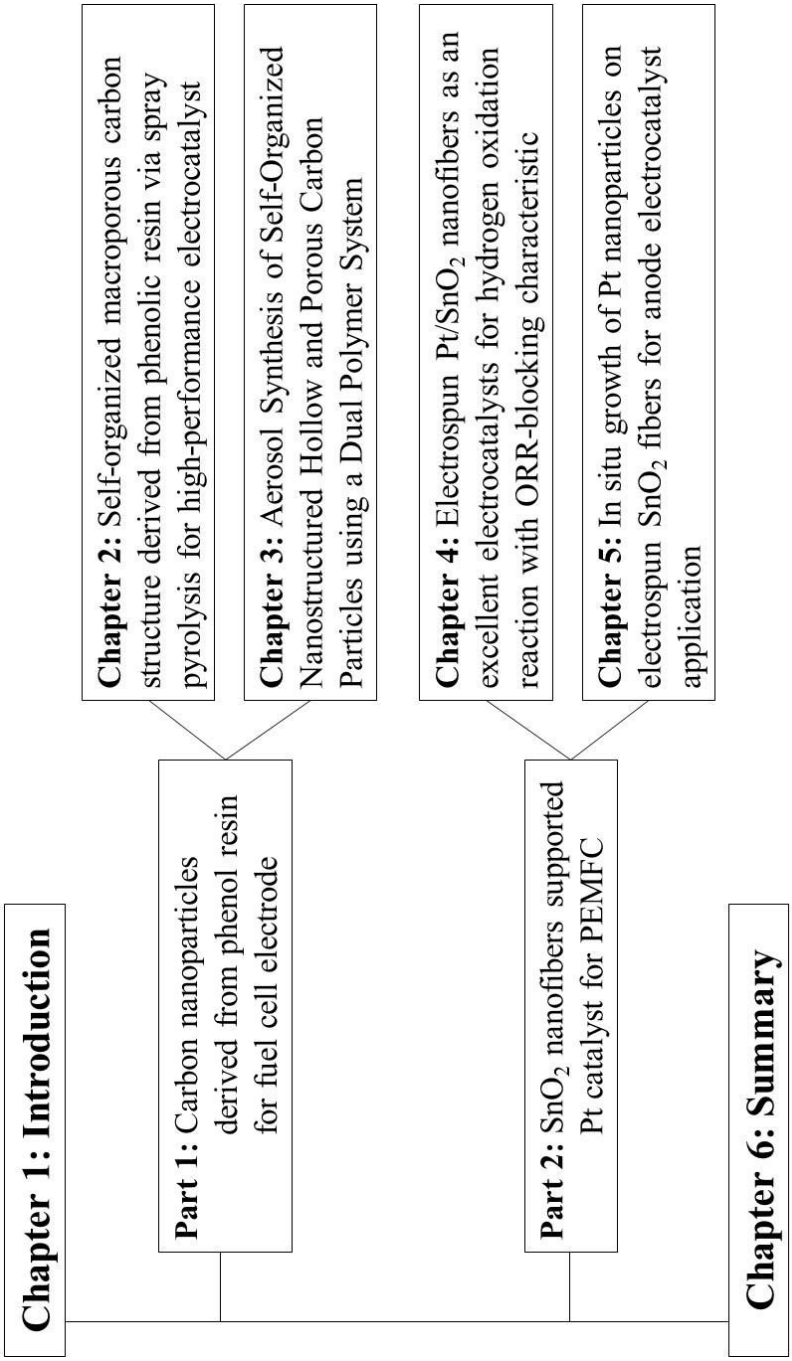

Fig. 1.6. Thesis outline.

The application of synthesized nanostructured materials in energy and environmental field was also reported here. Catalysts based on nanostructured materials have been developed. This thesis demonstrates various strategies for synthesis and application of nanostructured materials. A background and review of nanostructured materials and their applications were reported in the Chapter 1.

Chapter 2 describes the synthesis and evaluation of porous carbon derived from phenolic resin using a fast and facile spray pyrolysis method has been studied for use as a new electrocatalyst support material. By adding polystyrene latex nanoparticles as a template to the phenolic resin precursor, self-organized macroporous carbon structure was first developed. The mass ratio of phenolic resin to PSL at 0.625 gave the optimum porous morphology. Pt nanoparticles (~20 wt%) were grown on the carbon surface using a standard industrial impregnation method. Well-dispersed Pt nanoparticles of average size 3.91 nm were observed on the surface of porous carbon particles. The high catalytic performance of porous Pt/C electrocatalyst was confirmed by the high mass activity and electrochemically active surface area, which were 450.81 mA mg^{-1}-Pt and 81.78 m2 g^{-1}-Pt, respectively. The porous Pt/C catalyst obtains two times higher mass activity than that of the commercial Pt/C catalyst and performs excellent durability under acid conditions [12].

A novel strategy for designing the morphology of carbon nanoparticle has been performed from carefully study the role of template charge in organic–organic frameworks and reported in Chapter 3. An organic precursor containing electrically-charged polystyrene latex (PSL) and phenolic resin was ultrasonically sprayed followed by heating treatment to produce hollow or porous carbon nanoparticle.

A highly positive-charged PSL obtained hollow carbon nanoparticle, and degradation of zeta potential value of PSL obtained porous carbon nanoparticle [13].

Chapter 4 describes the synthesis of Pt/SnO_2 nanofibers via electrospinning. The unique electrochemical properties were in evidence based on the activity that allowed a hydrogen oxidation reaction and inhibit an oxygen reduction reaction. A high electrochemically active surface area value of 81.17 m^2/g-Pt was achieved with ultra-low Pt loading (4.03 wt%). The kinetics of a hydrogen oxidation reaction was investigated using a linear sweep voltammetry technique under a hydrogen atmosphere. A diffusion-limited current was achieved at 0.07 V and was stable at a high potential. This preparation technique shows great promise for the design of anode electrocatalyst material for fuel cells [14].

A facile method to synthesize Pt nanoparticles on the electrospun SnO_2 fiber matrix describes in Chapter 5. Precursors contained tin chloride pentahydrate, hexachloroplatinic acid, polyacrylonitrile, and N,N-dimethylformamide were electrospun and subsequently calcinations was carried out at 500 ^{o}C for 4h. It is shown that Pt nanoparticles were grown on SnO_2 fiber matrix without any formation of PtO. Pt nanoparticles size was in the range of 6–32 nm, by adjusting the concentration of polyacrylonitrile. The electrochemically active surface area of Pt/SnO_2 fibers was found to be very competitive compared to the commercially available electrocatalyst. This work demonstrates that Pt/SnO_2 fibers can be generated by a facile electrospinning process [15].

Chapter 6 summarizes the synthesis of nanostructured materials for catalyst application.

1.4. References

[1] A. C. Balazs, T. Emrick, T. P. Russel, Science 314, 1107 (2006).

[2] T. Hasell, J. Yang, W. Wang, J. Li, P. D. Brown, M. Poliakoff, E. Lester, S. M. Howdle, J. Mater. Chem. 17, 4382 (2007).

[3] M. E. Mackay, A. Tuteja, P. M. Duxbury, C. J. Hawker, B. V. Horn, Z. Guan, G. Chen, R. S. Krishnan, Science 311, 1740 (2006).

[4] K. M. Yun, A. B. Suryamas, C. Hirakawa, F. Iskandar, K. Okuyama, Langmuir 25, 11038 (2009).

[5] T. Ogi, A. B. D. Nandiyanto, K. Okuyama, Advanced Powder Technology, http://dx.doi.org/10.1016/j.apt.2013.11.005.

[6] Y. Xia, Y. Xiong, B. Lim, S. E. Skrabalak, Angew. Chem. Int. Ed. 48, 60 (2009).

[7] Z. M. Huang, Y. Z. Zhang, M. Kotaki, S. Ramakrishna, Compos. Sci. Technol. 63, 2223 (2003).

[8] K. Okuyama, D. D. Hung, J. H. Seinfeld, N. Tani, Y. Kousaka, Chem Eng. Sci. 46, 1545 (1991).

[9] S. Y. Lee, L. Gradon, S. Janeczko, F. Iskandar, K. Okuyama, ACS Nano 4, 4717 (2010).

[10] D. Li, Y. Xia, Adv. Mater. 16, 1151 (2004).

[11] Y. Garsany, O. A. Baturina, K. E. Swider-Lyons, S. S. Kocha, Anal. Chem. 82, 6321 (2010).

[12] R. Balgis, S. Sago, G. M. Anilkumar, T. Ogi, K. Okuyama, ACS Applied Materials & Interfaces 5, 11944 (2013).

[13] R. Balgis, T. Ogi, W.-N. Wang, G. M. Anilkumar, S. Sago, K. Okuyama, Langmuir

30, 11257 (2014).

[14] A. B. Suryamas, G. M. Anilkumar, S. Sago, T. Ogi, K. Okuyama, Catal. Commun. 33, 11 (2013).

[15] S. Sago, A. B. Suryamas, G. M. Anilkumar, T. Ogi, K. Okuyama, Mater. Lett. 105, 202 (2013).

Chapter 2

Self-Organized Macroporous Carbon Structure Derived from Phenolic Resin via Spray Pyrolysis for High-Performance Electrocatalyst

2.1. Introduction

The performance of an electrocatalyst relies strongly on its support material [1-3]. The design of electrocatalyst support materials therefore plays a crucial role in determining the overall electrocatalytic performance. The successful design of electrocatalyst support materials gives high-performance and reliable electrocatalysts [4-7]. Several types of electrocatalyst support materials are currently being studied such as carbonaceous materials, metal oxides, and nitrides [8-13].

Carbonaceous materials are favored because of the natural abundance of carbon, and they can be easily synthesized by the carbonization of various organic materials [14,15]. Much recent interest has been shown in the development of carbon-based catalysts produced using carbon black materials, such as Vulcan carbon, as a catalyst support [16-18]. The entire surface of Vulcan carbon is decorated with micropores giving a very high specific surface area ~250 m^2/g and large pore volume [19,20]. Although such microporous materials are used in catalysis applications, they have limitations arising from the slow mass transport of molecules because of space confinement imposed by small pore sizes, low conductivity arising from the presence of large numbers of surface functional groups and defects, and the collapse of porous structures in the harsh environment of proton exchange membrane fuel cell (PEMFC)

operation, which potentially trap and inactivate Pt nanoparticles [21].[21] Carbonaceous materials derived from organic materials offer morphological control by simply adding a specific template [22-26]. However the carbonization ratios of such materials are quite low, resulting in high-cost mass production. Recently, it has been found that inexpensive phenolic resin is more attractive as a carbon source because it has a high carbonization ratio [27,28].

The structural engineering of carbonaceous materials to give ultrafine spherical particles can be rapidly obtained using spray pyrolysis methods [29]. The use of silica as a sacrificial template for preparing hollow spherical carbon particles from phenolic resin by spray pyrolysis has been reported [30]. However, the functionalization of phenolic resin derived carbon particles has not yet been addressed. Functionalization of the controlled morphology of phenolic resin derived carbon for use as catalyst supports will provide more active Pt Nanoparticles and improve the chemical properties of the catalyst that will give catalysts exhibiting high electrocatalytic performances and good durabilities.

To the best of our knowledge, there have been no previous reports of the preparation of high-performance electrocatalysts consisting of Pt-nanoparticle-decorated macroporous carbon particles (porous Pt/C), derived from a phenolic resin via spray pyrolysis. Sacrificial template particles, i.e., polystyrene latex (PSL) that decompose easily during carbonization were chosen to control the morphology of the produced particles [4]. The obtained layered pores, which create channels inside the particles, could support a three-phase boundary (i.e. ion conducting phase, electron conducting phase, and gas phase). The use of multistep stacking of temperature zones in the spray pyrolysis reactor controls the formation of the phenolic resin/PSL composite and the

carbonization process. Morphological control of the carbon was investigated in detail by changing the ratio of phenolic resin to PSL. We carried out cyclic voltammetry (CV) and an oxygen reduction reaction (ORR) on the materials to determine their electrochemical properties.

2.2. Experiment

Preparation of Porous Pt/C Electrocatalyst. An aqueous solution containing phenolic resin (Sumitomo Bakelite Co., Ltd., Tokyo, Japan) and 4 wt% of laboratory-produced PSL (230 nm) beads were used as a precursor to prepare carbon particles by spray pyrolysis. The spray pyrolysis apparatus consisted of an ultrasonic nebulizer (1.7 MHz, NE-U17, Omron Healthcare Co., Ltd., Kyoto, Japan) for droplet generation, a tubular furnace, and an electrostatic precipitator, as shown in Figure 1. The tubular furnace consisted of five stacked temperature zones set at 150, 300, 700, 700, and 700 °C, respectively. The mass ratio of phenolic resin to PSL was 5, 2.5, 1.25, 0.625, and 0.25. The Pt impregnation process has been described in our earlier work [4]. The process was repeated here.

Characterization. The particle morphology was observed using field-emission scanning electron microscopy (FE-SEM; S-5000, 20 kV, Hitachi High-Tech. Corp., Tokyo, Japan) and transmission electron microscopy (TEM; JEM-2010, 200 kV, JEOL Ltd., Tokyo, Japan). The thermal behaviors of the phenolic resin, the phenol–PSL composite, and PSL were analyzed using thermogravimetric analysis (TGA; TGA-50/51, Shimadzu Corp., Kyoto, Japan). The surface area was determined using Brunauer, Emmet, and Teller (BET) method (BEL Japan, Inc., BELSORP-max, Osaka, Japan). Fourier-transform infrared (FT-IR) spectroscopy was used to investigate the chemical

reactions involved in phenol carbonization (Spectrum one, Perkin Elmer Inc., Waltham, MA, USA). The Pt content of the catalyst was measured using inductively coupled plasma mass spectrometry (SPS-3000, Seiko Instrument Inc., Chiba, Japan). The crystal structure was determined using X-ray diffraction (XRD; RINT2000, Rigaku, Tokyo, Japan).

Electrochemical characterization of the prepared catalyst was performed using CV and a rotating disc electrode (RDE; HR-301, Hokuto Denko Corp., Tokyo, Japan). A reversible hydrogen electrode (RHE) was used as the reference electrode for these measurements. Catalyst ink was prepared using a procedure reported elsewhere [4]. The required amount of catalyst ink was transferred to a polished glassy carbon disk (⌀ = 5 mm, geometric area = 0.196 cm^2) and dried to form a thin catalyst layer. The measurements were performed at room temperature (~25 °C) using a freshly prepared 0.1 M $HClO_4$ electrolyte solution (Cica-reagent, Kanto Chemical Co., Inc., Japan). A nitrogen gas flow of 100 mL min^{-1} was passed through the electrolyte solution for 30 min before measurements to deoxygenate the environment. CV measurements were obtained by scanning between 0 and 1.2 V vs RHE at a sweep rate of 50 mV s^{-1}. The saturating gas was switched to oxygen for the RDE measurements, and the electrolyte was saturated using the same conditions as those used for the CV measurements. The rotation rates were controlled at 400, 900, 1600, 2500, and 3600 rpm to collect data for Koutecký–Levich plots. Measurements were carried out at sweep rates of 10 mV s^{-1} in a typical polarization program of 0.2 V → 1.2 V. The background current was measured by running the ORR sweep profile without any rotation in nitrogen gas purged 0.1 M $HClO_4$ before the ORR measurements to eliminate any contributions from capacitive current.

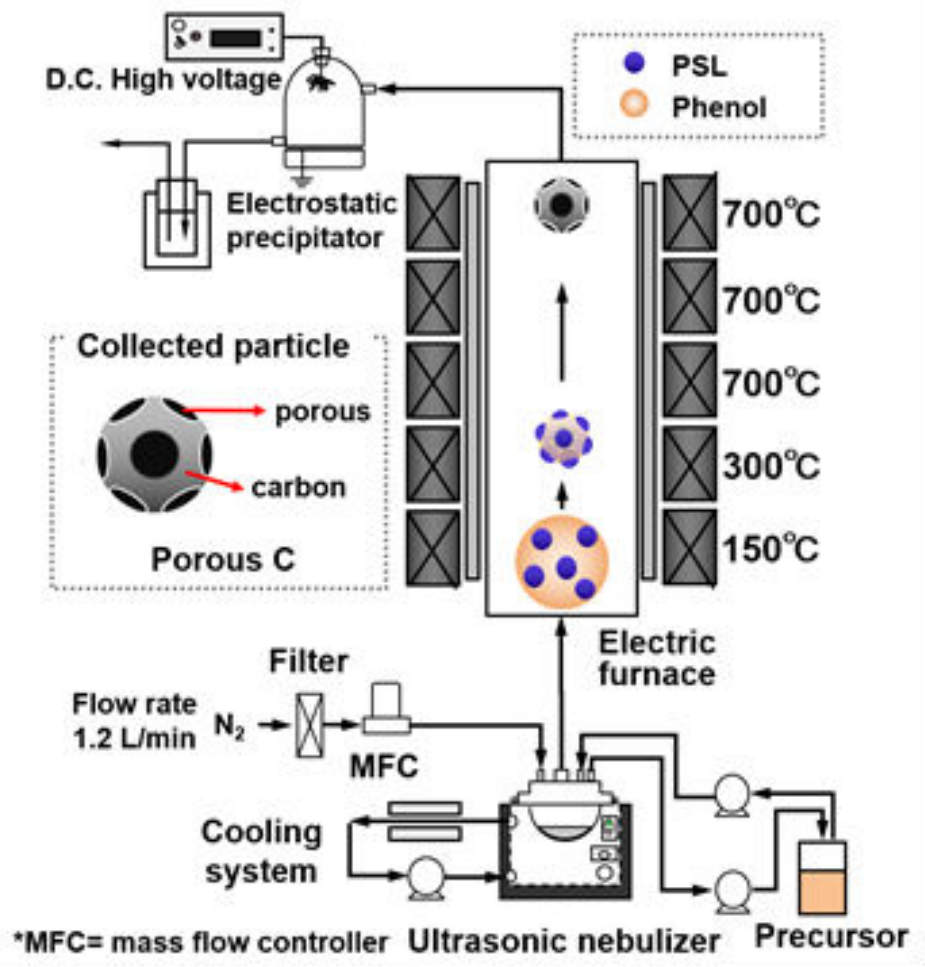

Fig. 2.1. Schematic diagram of the experimental setup.

2.3. Results and Discussions

The thermal behaviors of the phenolic resin, PSL, and phenolic resin–PSL composite were examined at the temperature of 20−800 °C under a nitrogen atmosphere as shown as TGA curves in Figure 2. There were four stages observed in the TGA curve of the phenolic resin. The first stage was up to 150 °C showed a weight loss of less than ca. 10 %. The second and third stages were up to 600 °C indicated two continuous weight decreases and represented the main degradation reaction of ca. 20 %. Above 600 °C (the fourth stage) ca. 8% weight loss was observed. The weight loss during this

heat treatment is ascribed for the release of various gases (CO, CO_2, CH_4, and H_2) and H_2O evaporation depending on the decomposition state of phenolic resin [31]. The carbonized material was relatively stable in the final step with the lowest weight loss because carbonization had already been achieved. In the case of PSL, the TGA result shows sharp weight degradation at 350 °C and all of the PSL were completely decomposed at 400 °C.

The initial stage of TGA curve of the phenolic resin–PSL composite indicated a similar weight loss as phenolic resin case. However, a sharp weigh loss was observed in the range of 400–450 °C, implying rapid PSL decomposition. A very small decomposition was then presented at 450–600 °C and the weight become stable at the above temperature.

It is to be noted from the TGA results that the large shift of the decomposition temperature of PSL in phenolic resin-PSL composite toward higher temperature (ΔT ~50 °C) compared to that of pure PSL particle, indicates the strong interaction formation between phenolic resin and PSL surface. The interaction may be due to the chemical bonding between the OH groups of the phenolic resin and the CN groups on the surface of PSL nanoparticles as described later. Then, the effect of this interaction on the macroporous morphology of carbon particles was examined for several mixing composition by the spray pyrolysis method as follows.

Figure 3 shows the effect of phenolic resin concentration on the carbon particle morphology; the concentration of PSL was fixed at 4 wt% and the amount of phenolic resin was varied, i.e., 0.1, 0.25, 0.5, 1, and 2 wt%. A PSL sol (1 mL) was added per 10 mL of phenolic resin solution. We found that the porosity decreased with increasing amounts of phenolic resin. Similar phenomenon was shown elsewhere [32]. Adjustment

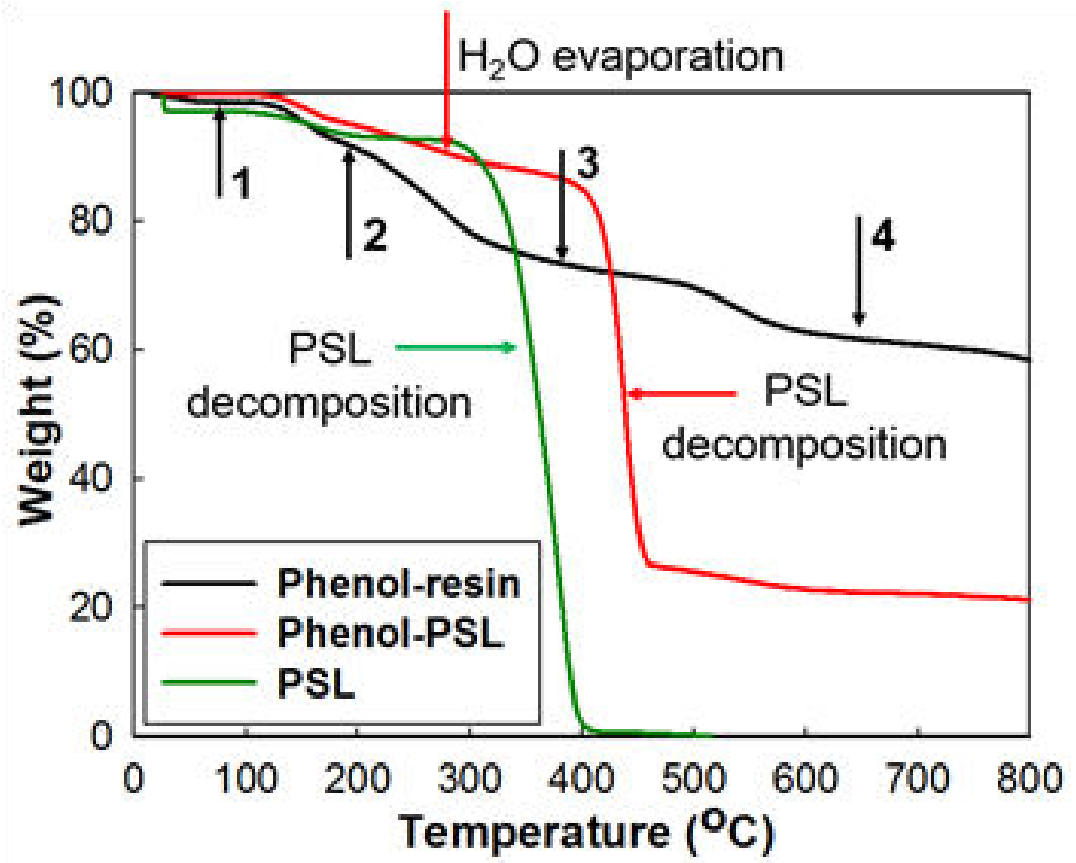

Fig. 2.2. TGA thermograms of the phenolic resin, phenolic resin–PSL composite, and PSL.

of the porous structure of the catalyst support was critical for effective gas/water diffusion and proton/electron transport to and from the catalytic sites without sacrificing the sites for Pt deposition. Figure 3(c)–(e) show poorly structured porous morphologies, which tend to be dense when the amount of phenolic resin is high. This provides many sites for Pt deposition on the outer surfaces of the carbon particles, but not on the inner surfaces because the pore sizes of the carbon particles are unsuitable and inhibit Pt ion penetration. Low phenolic resin concentrations gave good catalyst support as a result of the presence of pore channels, as shown in Figure 3(a) and (b). The highest porosity of the carbon particles was obtained at a phenolic resin concentration of 0.1 wt%, as shown

in Figure 3(a). This enables the best fluid transport through the catalytic sites. However, since most of the carbon surface was occupied by macropores, there were only a small number of sites that could be used for Pt deposition. Furthermore, the Pt nanoparticles potentially agglomerate during the deposition process. The optimum porous morphology was obtained at a phenolic resin concentration of 0.25 wt%, as shown in Figure 3(b). This porous morphology provided a good combination of fluid transport and Pt deposition sites. Fluid transport occurs effectively and Pt can be deposited both on the outer and inner surfaces of the carbon, which means that a higher number of active catalytic sites can be achieved. The specific surface area (S_{BET}) of this porous carbon was 107 m^2 g^{-1}. Figure 3(f) shows the probable phenomena that occur during Pt deposition on the surface of microporous and macroporous carbon.

The beautiful formation of self-organized macroporous carbon obtained at a phenolic resin concentration of 0.25 wt%, as shown in Figure 3(b) may be due to the chemical interaction between phenolic resin and PSL. Therefore, the chemical structure of porous-carbonized sample and the PSL were further investigated. FT-IR spectra were obtained and are shown in Figure 4. In the FT-IR spectrum of PSL, alkyl (C_nH_{2n+1}) groups was found in the range of 600−1000 and 1400−1700 cm^{-1}. Sharp peak at 3033 cm^{-1} and double peaks at 2921 and 2848 cm^{-1} correspond to the C-H stretching mode. Polar group of C-N stretch was indicated by peak at 1221 cm^{-1}. In the case of porous-carbonized sample, a weak broad peak was observed at 3350 cm^{-1} indicating the presence of OH···OH, OH···O (ether oxygen), or OH···O=C hydrogen bonds. An aromatic bond from benzene was indicated by a weak peak at 3070 cm^{-1}. The weak peak at 3000 cm^{-1} indicated the presence of –OH bonds. An aromatic ring C-C bond was also present as indicated by the strong peak at 1600 cm^{-1}. A strong peak at 1320 cm^{-1} that

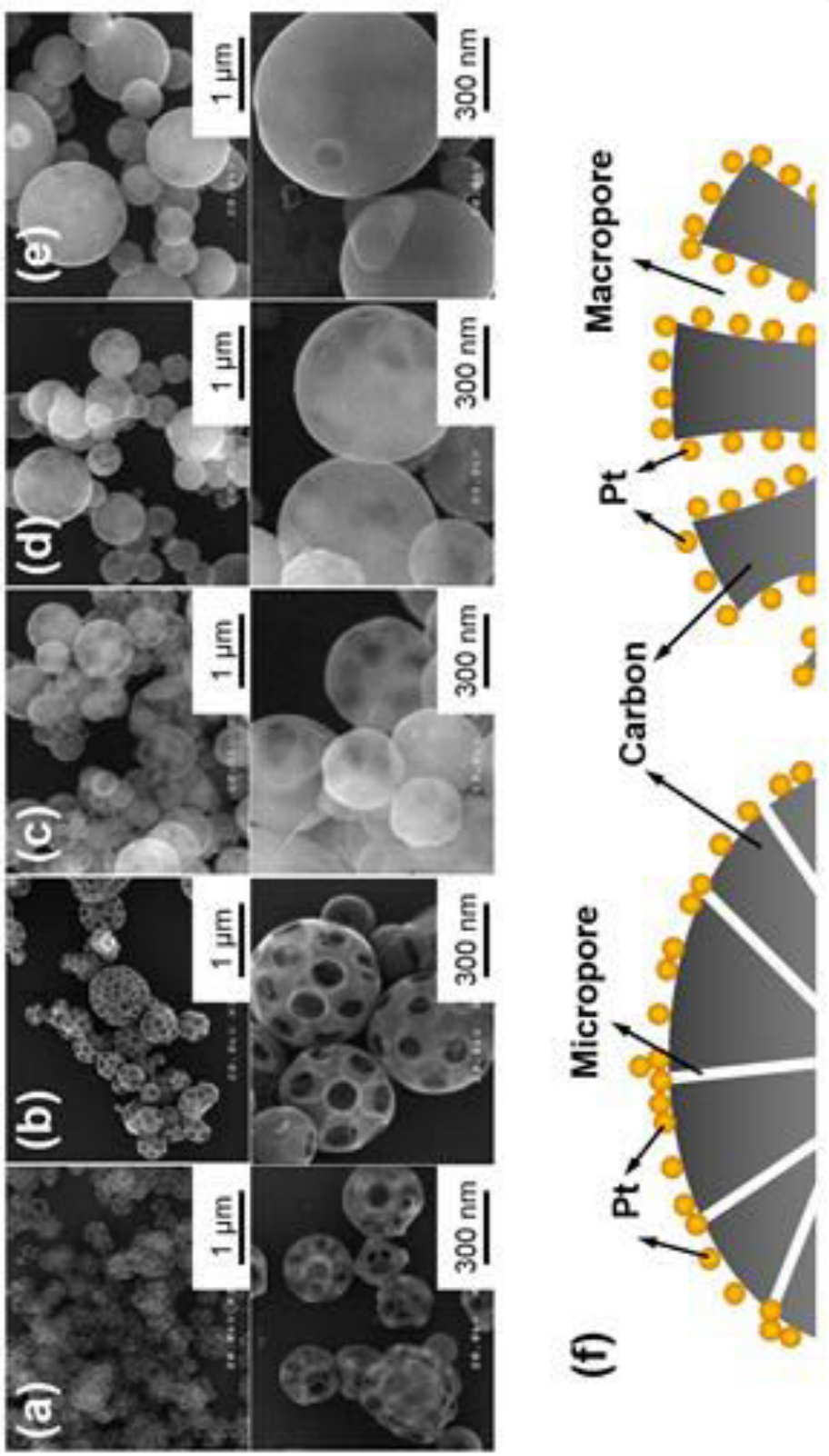

Fig. 2.3. FE-SEM image of porous carbon using 4 wt% P^+ and phenol resin concentrations of (a) 0.1, (b) 0.25, (c) 0.5, (d) 1, and (e) 2 wt%; and (f) schematic diagram of Pt deposition phenomena on the surfaces of microporous and macroporous carbon.

corresponds to a C-O stretching vibration was found for the carbonized sample [31,33,34]. This peak is not present in Vulcan XC-72 carbon, as reported by Li et al [35]. This peak shows that a large amount of unsaturated carbon atoms are present and these are highly active toward reaction with oxygen and form oxygen-containing group that may enhance the ORR activity [35]. These results indicated that the interaction between PSL and phenolic resin is due to the hydrogen bonding and electrostatic bonding among polar groups such as C-N, -OH, and C=O groups.

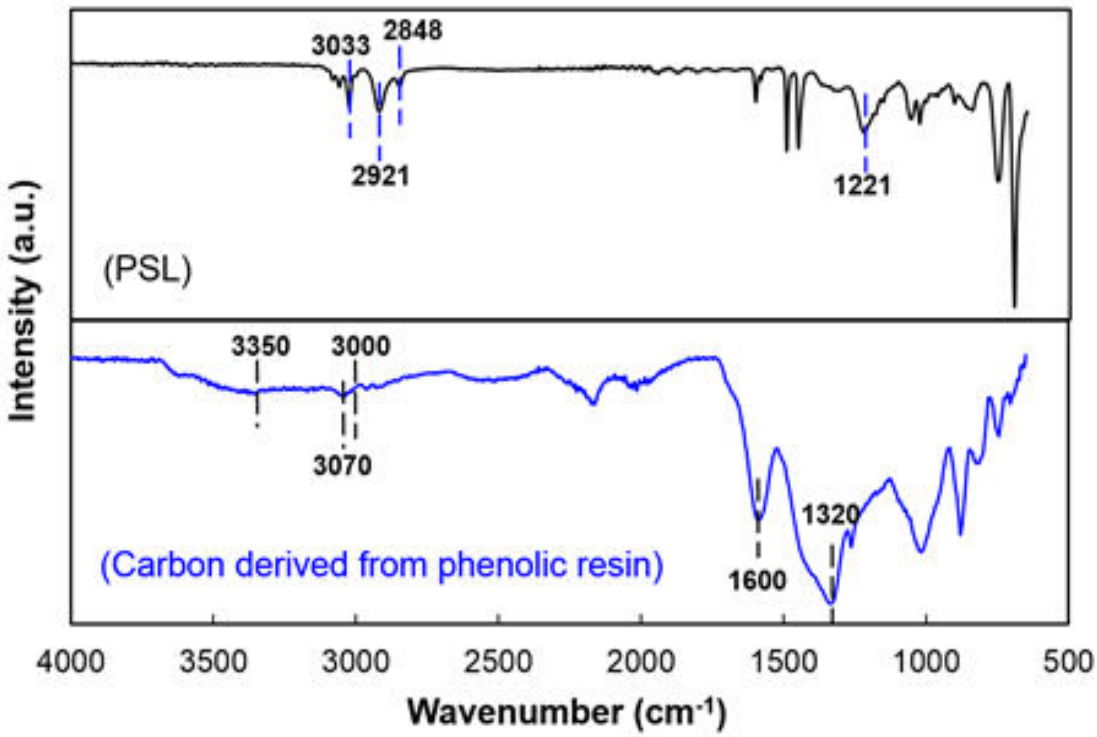

Fig. 2.4. FT-IR spectra of the PSL and phenolic resin derived carbon.

Functionalization of porous carbon as a catalyst support was performed by Pt impregnation (~20 wt%) to the porous carbon surface, and was mediated by PVA. Figure 5(a) and (b) show FE-SEM images of the porous Pt/C particles. These images confirm the presence of Pt nanoparticles on the porous carbon surfaces and show that

the carbon particles have strong structures and their morphology is maintained as spherical porous particles after Pt deposition. The carbon particles have well-structured pores with specific angles and, interestingly, agglomeration-free Pt nanoparticles deposited on the inner surfaces of the carbon particles and in the cavities, as shown clearly by the TEM images in Figure 5(c) and (d). Figure 5(e) confirms that the deposited Pt is well-dispersed. The surfaces of the deposited Pt nanoparticles are clean and the nanoparticles form a crystal structure, as shown by the clear lattice spacing. The mean diameters of the Pt nanoparticles were calculated using 280 Pt nanoparticles and found to be 3.91 nm with a standard deviation of about 0.67 nm, as shown by the histogram in Figure 5(f). The amount of Pt nanoparticles in the porous carbon was confirmed by ICP measurements and found to be 18.9 wt%, which is slightly different to that in the prepared precursor. Small amounts of Pt were lost during Pt deposition and washing.

Figure 5(g) shows the XRD pattern of the porous Pt/C catalyst. The XRD pattern has broad peaks at 25° (2θ) corresponding to the diffraction of amorphous carbon. The diffraction peaks of Pt are present at 39°, 46°, and 68° (2θ), which corresponds to the (111), (200), and (220) crystalline planes, respectively (JCPDS Card No. 4-0802), with a face-centered cubic crystal structure. The crystallite size of the Pt nanoparticles was calculated using the Scherrer equation and found to be 4.21 nm. The Pt crystallite size was almost equal to the Pt nanoparticle diameter; this was calculated using the TEM images. The Pt diffraction peaks proved that the reduction of chloroplatinic acid by sodium borohydride had been achieved.

To discover the effect of catalyst support` pore size to the Pt deposition, Pt nanoparticles were also deposited on the microporous carbon. The obtained deposition

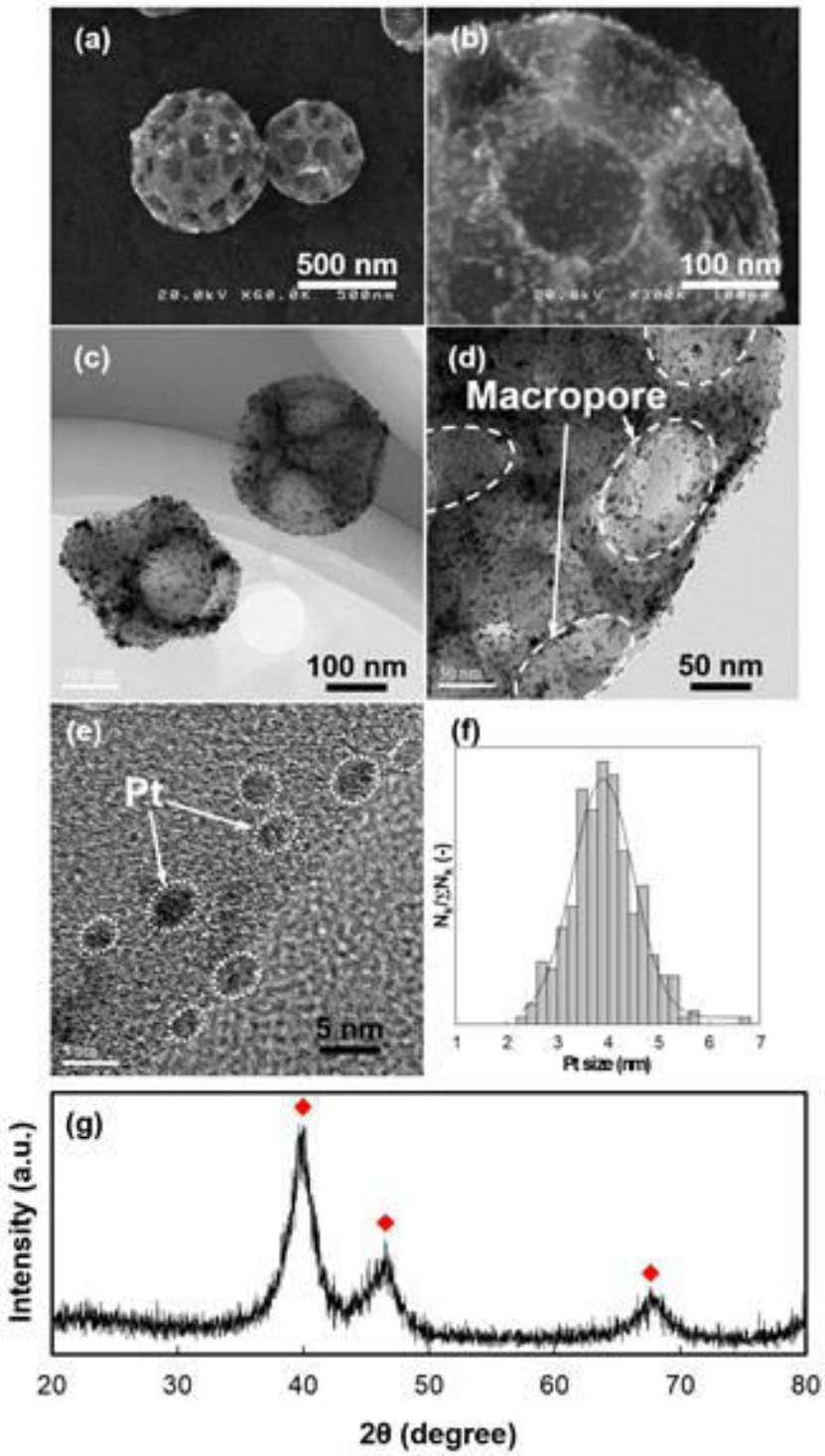

Fig. 2.5. (a), (b) FE-SEM images of the porous Pt/C catalyst, (c), (d) TEM image of the porous Pt/C catalyst, (e) HR-TEM image of the distribution of 20 wt% Pt on the carbon surface, (f) histogram of Pt nanoparticle distribution, and (g) XRD patterns of the porous Pt/C catalyst after reheating at 120 °C for 120 min under vacuum.

phenomena were totally different from that of on the macroporous carbon, as shown from the FE-SEM images of Figure 6. Pt nanoparticles were growth locally and highly agglomerated. Even though microporous Pt/C catalysts were prepared using exactly the same method as macroporous Pt/C, and the amount of Pt loading was also the same ~20 wt%. This phenomenon agreed the previous prediction on the effect of catalyst support` pores to the Pt nanoparticles deposition that was presented in Figure 3(f).

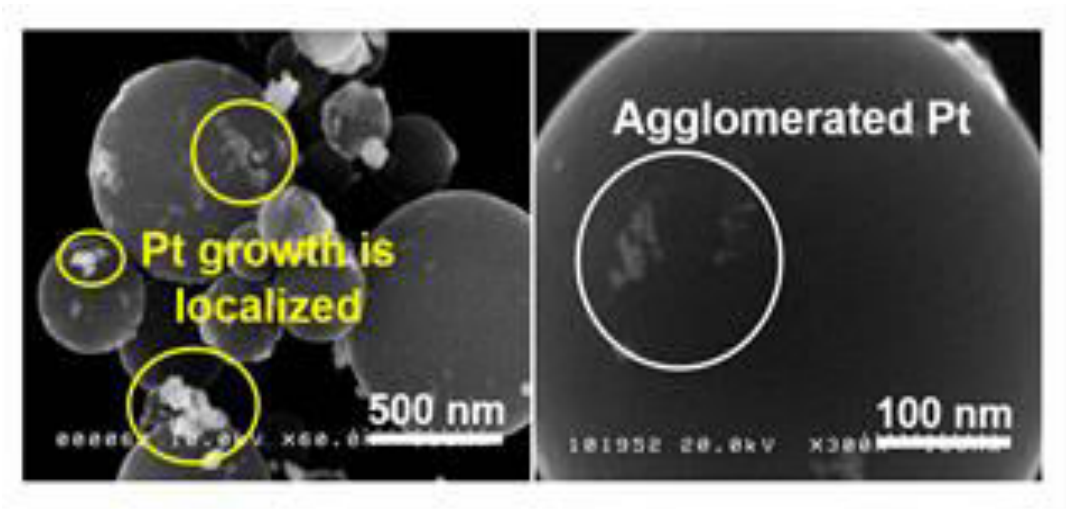

Fig. 2.6. FE-SEM images of microporous Pt/C catalyst.

Electron tomography (ET) images of the porous Pt/C catalyst are shown in Figure 7. The red, green, and blue axes represent the *x*-, *y*-, and *z*- axes, respectively. The presence of C and Pt atoms in the observed particles are shown in blue and red, respectively, while green shows the transition from each Pt area to C area. Figure 7(a) shows that the catalyst is highly porous and the pores have an interconnected system. Furthermore, Pt nanoparticles were well-dispersed over the entire carbon surface including the inside of the pores. A slice of the ET image taken at $z = r$ (r is the radius of the observed sample) is shown in Figure 7(b). It is clear that pore space is present inside the catalyst. This observation confirms that the prepared porous catalyst offers effective

fluid transport and it may also have an enhanced Pt nanoparticles active surface. Figure 7(c) shows reconstructed 3D-TEM images of the synthesized porous Pt/C catalyst. This image shows that the catalyst particle contained macropores in addition to many small pores that clog each other and form a layer with "crumpled graphene-like" morphology. This is advantageous from an active surface area point of view and another reason why Pt nanoparticles are well-dispersed in this catalyst support.

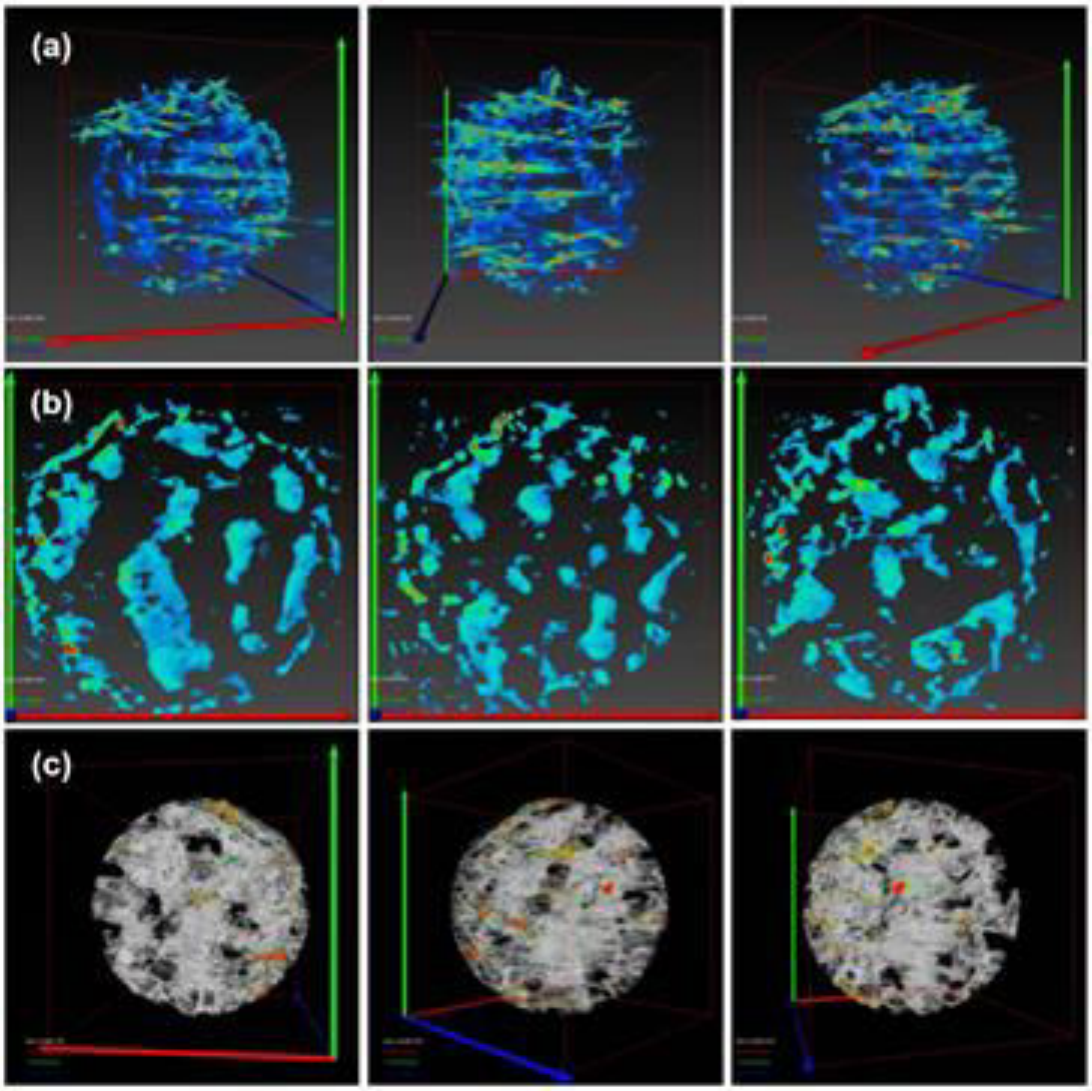

Fig. 2.7. Electron tomography (ET) images of the porous Pt/C catalyst: (a) in the x, y, and z directions, (b) in the x and y directions, and (c) after the reconstruction process.

The electrochemical properties of the prepared porous Pt/C catalyst were determined using CV and ORR polarization curves. In addition, the electrochemical properties of a commercial Pt/C catalyst (46.1 wt%, purchased from Tanaka Kikinzoku Kogyo Co., Ltd., Tokyo, Japan) were also evaluated to determine the figure of merit of the prepared catalyst. Figure 8(a) shows the typical hydrogen adsorption/desorption characteristics of both porous Pt/C and commercial Pt/C at the 10th measurement cycle. The electrochemically active surface areas (ECSAs) of Pt in the working electrode were found to be 81.78 and 80.47 m^2 g^{-1}-Pt for the prepared and the commercial catalyst, respectively. The ECSAs were calculated using the hydrogen adsorption charge ($Q_{H\text{-adsorption}}$) area limited by the minimum potential, which was just above the potential of H_2 generation onset (between 0.07 to 0.4 V vs RHE). The prepared catalyst had a comparable ECSA even though the Pt loading was much less than that of the commercial catalyst. In addition, the Pt size of the prepared catalyst (~3.9 nm) was twice that of the commercial catalyst (~2 nm).

Typical ORR curves of the prepared and commercial Pt/C catalyst, measured after the 10th CV cycle are shown in Figure 8(b). The ORR curves for the porous Pt/C recorded at different rotation speeds are shown in Figure 8(c). These measurements were performed to obtain Koutecký–Levich plots (Figure 8(d)) to calculate the number of electrons transferred during O_2 reduction and to evaluate the mass and specific activities using the limiting current method. The target potential for the calculation of the mass activity and the specific activity was quantified at E = 0.9 V. The number of electrons involved in the ORR was calculated using the Koutecký–Levich equation and 4 electrons were involved for both the prepared porous Pt/C and the commercial Pt/C catalyst. Pt mass activity values were calculated by normalizing the Pt loading on the

disk electrode and the specific activity values were estimated by calculating the mass–specific activities and normalizing them to the Pt ECSA. The high quality of the catalyst is shown by its high electrocatalytic activity. The mass activity value under the initial condition (10 cycles) was 450.81 mA mg^{-1}-Pt whereas the specific activity value was 551.24 μA cm^{-2}-Pt. These values were twice those of the commercial Pt/C catalyst,

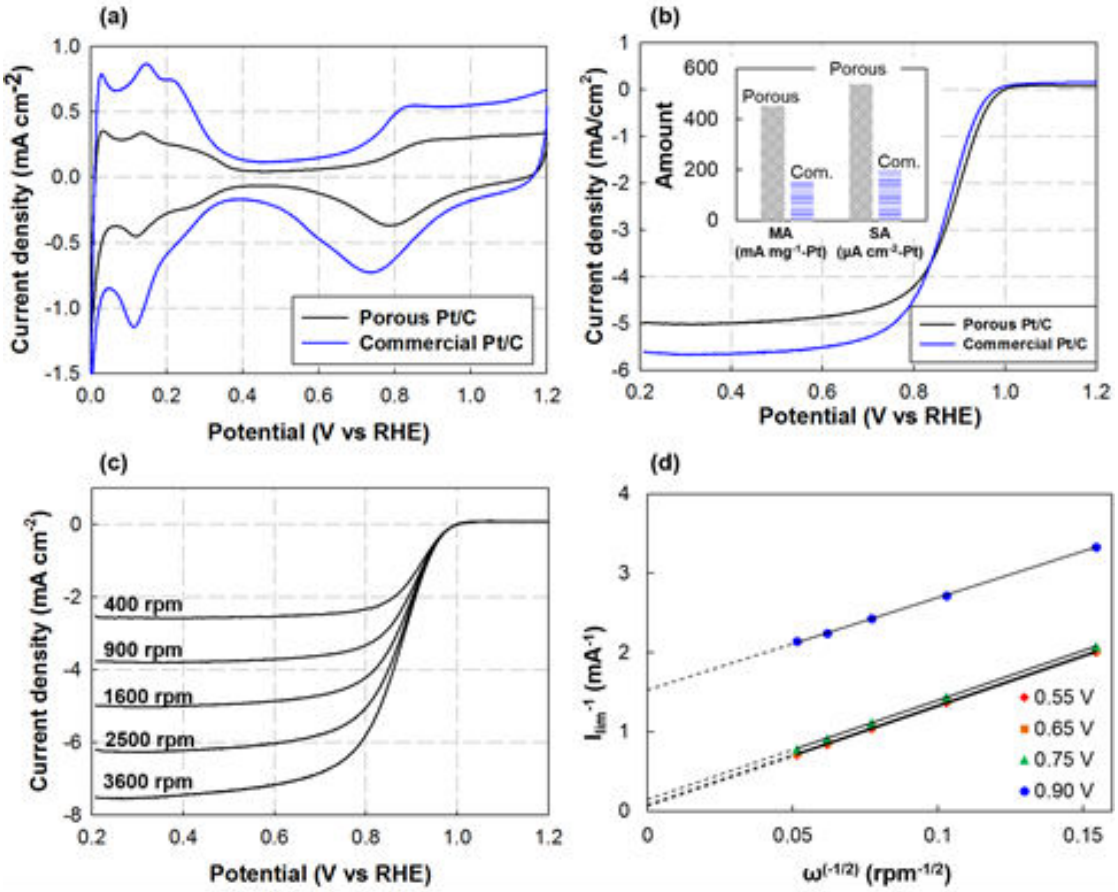

Fig. 2.8. (a) CVs of the porous Pt/C catalyst and the commercial Pt/C catalyst over 10 cycles in oxygen-free 0.1 M $HClO_4$ (cycling between 0 and 1.2 V at 50 mV s^{-1} sweep rate), (b) comparison of the ORR polarization curve of the porous Pt/C catalyst and the commercial Pt/C catalyst at a rotation rate of 1600 rpm, (c) ORR polarization curves at different rotation rates for the porous Pt/C catalyst after 10 cycles in oxygen-saturated 0.1 M $HClO_4$ at a sweep rate of 10 mV s^{-1}, and (d) Koutecký-Levich plot of the porous Pt/C catalyst at different rotation rates and potentials.

which was about 155.00 mA mg^{-1}-Pt and 192.61 μA cm^{-2}-Pt for the mass activity and the specific activity, respectively. The values for the mass activities and the specific activities of the prepared sample and the commercial Pt/C are summarized in the inset of Figure 8(b).

Electrocatalytic activity measurements for both catalysts were conducted over 10,000 cycles to determine their durability. Over the first 1000 cycles the porous Pt/C had a relatively more stable ECSA than the commercial catalyst with total degradations of 23.45 and 29.51% for porous Pt/C and commercial Pt/C, respectively. Because the performance of the commercial Pt/C was already low in this step, only the porous Pt/C catalyst was used for further durability testing. Typical CV polarization curves of the prepared catalyst at the 10th and $10{,}000^{th}$ cycles are shown in Figure 9. The CV curve at the $10{,}000^{th}$ cycle was smaller than that measured at the 10th cycle. However, there was no change in the shape of the polarization curve showing that hydrogen adsorption/desorption still took place even at the $10{,}000^{th}$ cycle. This means that there are no significant carbon particle breakages during the durability measurements even though some Pt agglomeration occurred. After 10,000 cycles the ECSA only decreased by 35.17% and its value was 53.11 m^2 g^{-1}-Pt. The mass activity and specific activity were 219.43 mA mg^{-1}-Pt and 413.20 μA cm^{-2}-Pt, respectively. Although a fairly high level of degradation was evident the electrocatalytic activity values were still higher than those of the commercial catalyst. This phenomenon proves that phenolic resin derived carbon has good durability under acidic conditions. Phenolic resin derived carbon may have strong corrosion resistance that maintains the active catalyst.

The 3.91 nm particle size observed on the as-prepared porous carbon supports is large compared with those typically observed on commercial carbon (~2 nm). This

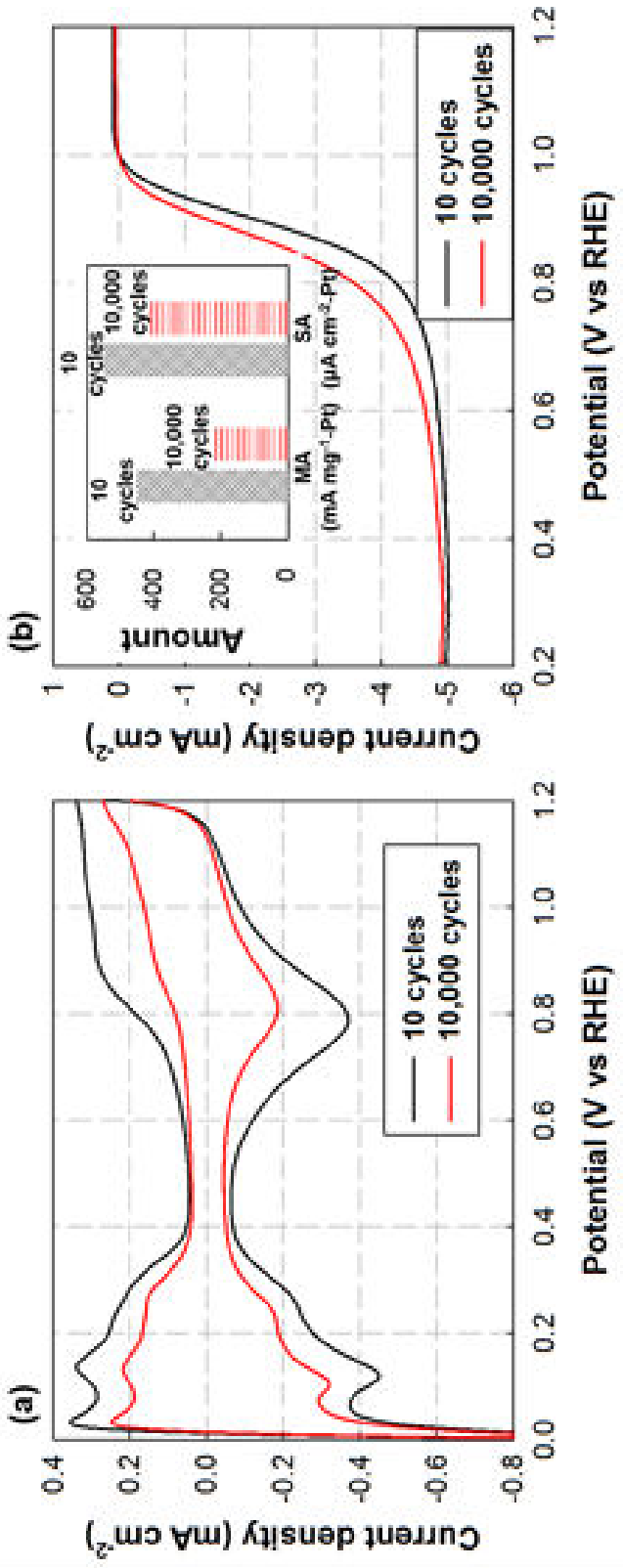

Fig. 2.9. (a) CVs of the porous Pt/C catalyst over 10 and 10,000 cycles in oxygen-free 0.1 M $HClO_4$ (cycling between 0 and 1.2 V at 50 mV s^{-1} sweep rate), (b) ORR polarization curve of the porous Pt/C catalyst over 10 and 10,000 cycles at a rotation rate of 1600 rpm.

finding suggests that Pt size is not the only important requirement to obtain high electrocatalytic activity. Carbon as a catalyst support also plays a role and is as important as the Pt catalyst. Carbon derived from phenolic resin, which contains various aromatic structures exhibits good electronic conductivity [28]. The obtained carbon morphology also consists of several layers, which increases the active surface area. A combination of the above two factors and the control of morphology to give macroporous–nanosphere particles increases the electrical conductivity of the prepared catalyst, and the above findings are first discussed in this work.

2.4. Conclusions

This study demonstrated a facile strategy for the production of a novel electrocatalyst support material, i.e., porous carbon derived from phenolic resin using spray pyrolysis. The morphology of the phenolic resin derived carbon was controlled simply by the addition of appropriate amount of PSL template particles to the precursor. Pt deposition on the phenolic resin derived carbon was achieved using a standard industrial impregnation method. Agglomeration-free and well-dispersed Pt nanoparticles of average size 3.91 nm were observed on the surfaces of the porous carbon particles. The high performance of the porous Pt/C electrocatalyst was proven by its high mass activity and electrochemically active surface area, which were 450.81 mA mg^{-1}-Pt and 81.78 m^2 g^{-1}-Pt, respectively. The porous Pt/C mass activity value is twice those of the available commercial Pt/C catalyst.

2.5. References

[1] H. Chang, S. H. Joo, C. Pak, J. Mater. Chem. 17, 3078 (2010).

[2] S. Zhang, Y. Shao, G. Yina, Y. Lin, J. Mater. Chem. A 1, 4631 (2013).

[3] E. Antolini, Appl. Catal., B 88, 1 (2009).

[4] R. Balgis, G. M. Anilkumar, S. Sago, T. Ogi, K. Okuyama, J. Power Sources 203, 26 (2012).

[5] R. Balgis, G. M. Anilkumar, G. M.; Sago, T. Ogi, K. Okuyama, Fuel Cells 12, 665 (2012).

[6] R. Balgis, G. M. Anilkumar, G. M.; Sago, T. Ogi, K. Okuyama, J. Power Sources 229, 58 (2013).

[7] S. H. Joo, S. J. Choi, I. Oh, J. Kwak, Z. Liu, O. Terasaki, R. Ryoo, Nature 412, 169 (2001).

[8] R. Kou, Y. Shao, D. Mei, Z. Nie, D. Wang, C. Wang, V. V. Viswanathan, S. Park, I. A. Aksay, Y. Lin, Y. Wang, J. Liu, J. Am. Chem. Soc. 133, 2541 (2011).

[9] Y. Zheng, Y. Jiao, J. Chen, J. Liu, A. Du, W. Zhang, Z. Zhu, S. C. Smith, M. Jaroniec, G. Q. Lu, S. Z. Qiao, J. Am. Chem. Soc. 133, 20116 (2011).

[10] A. B. Suryamas, G. M. Anilkumar, S. Sago, T. Ogi, K. Okuyama, Catal. Commun. 33, 11 (2013).

[11] K. Kakinuma, Y. Wakasugi, M. Uchida, T. Kamino, H. Uchida, S. Deki, M. Watanabe, Electrochim. Acta 77, 279 (2012).

[12] T. Ogi, R. Balgis, K. Okuyama, N. Tajima, H. Setyawan, AIChE J. 59, 2753 (2013).

[13] B. Avasarala, T. Murray, W. Li, P. Haldar, J. Mater. Chem. 19, 1803 (2009).

[14] H. Chang, S. H. Joo, C. Pak, J. Mater. Chem., 17, 3078 (2007).

[15] S. Xu, G. Qiao, H. Wang, D. Li, T. Lu, Mater. Lett. 62, 3716 (2008).

[16] B. Fang, N. K. Chaudhari, M.-S. Kim, J. H. Kim, J.-S. Yu, J. Am. Chem. Soc. 131, 15330 (2009).

[17] Y. Garsany, A. Epshteyn, A. P. Purdy, K. L. More, K. E. J. Swider-Lyons, Phys. Chem. Lett. 1, 1977 (2010).

[18] C. Koenigsmann, A. C. Santulli, K. Gong, M. B. Vukmirovic, W.-P. Zhou, E. Sutter, S. S. Wong, R. R. Adzic, J. Am. Chem. Soc. 133, 9783 (2011).

[19] D. R. Rolison, Science 299, 1698 (2003).

[20] B. Güvenatama, B. Fıçıcılar, A. Bayrakçekenb, I. Eroğlu, Int. J. Hydrogen Energy 37, 1865 (2012).

[21] C. Liang, Z. Li, S. Dai, Angew. Chem., Int. Ed. 47, 3696 (2008).

[22] Z. Wang, F. Li, N. S. Ergang, A. Stein, A. Chem. Mater. 18, 5543 (2006).

[23] H. Yoo, J. H Moon, RSC Adv. 2, 8934 (2012).

[24] B. Hu, K. Wang, L. Wu, S.-H. Yu, M. Antonietti, M. M. Titirici, Adv. Mater. 22, 813 (2010).

[25] M. Inagaki, H. Orikasab, T. Morishita, RSC Adv. 1, 1620 (2011).

[26] C. Liang, S. Dai, J. Am. Chem. Soc. 128, 5316 (2006).

[27] J. Ryu, Y.-W. Suh, D. J. Suh, D. J.; Ahn, Carbon 48, 1990 (2010).

[28] G. Guan, K. Kusakabe, H. Ozono, M. Taneda, M. Uehara, H. Maeda, J. Mater. Sci. 42, 10196 (2007).

[29] X. Xue, T. Lu, C. Liu, W. Xing, Chem. Commun. 1601 (2005).

[30] X. Yu, S. Ding, Z. Meng, J. Liu, X. Qu, Y. Lu, Z. Yang, Colloid Polym. Sci. 286, 1361 (2008).

[31] Y. J. Kim, M. I. Kim, C. H. Yun, J. Y. Chang, C. R. Park, M. J. Inagaki, Colloid

Interface Sci. 274, 555 (2004).

[32] A. B. D. Nandiyanto, O. Arutanti, T. Ogi, F. Iskandar, T. O. Kim, K. Okuyama, Chem. Eng. Sci. 101, 523 (2013).

[33] J.-G. Li, C.-Y. Chung, S.-W. Kuo, J. Mater. Chem. 22, 18583 (2012).

[34] Z. Wu, Y. Meng, D. Zhao, Microporous Mesoporous Mater. 128, 165 (2010).

[35] Y. Li, J. Wang, D. Geng, R. Li, X. Sun, Chem. Commun. 47, 9438 (2011).

Chapter 3

Aerosol Synthesis of Self-Organized Nanostructured Hollow and Porous Carbon Particles using a Dual Polymer System

3.1. Introduction

Carbon particles with hierarchical nanostructures are of great scientific interest due to their remarkable properties such as high specific surface area and porosity those enable their use in adsorbents, drug/gene carriers, super capacitors, fuel cells, and lithium batteries [1-4]. A careful structuring strategy is highly desirable yet very challenging to design the nanostructures of carbon particles. Many efforts have been extended to develop several liquid and gas-based processes to meet this challenge. In general, nanostructured carbon particles are prepared by using inorganic materials, such as mesoporous silica particles as a template, and organic materials as a carbon source that fills the voids between the templates [5-7]. To remove the inorganic templates, however, corrosive chemicals, such as hydrofluoric acid, are commonly used, which greatly limits its industrial applications [8,9]. Therefore, the use of organic templates that readily decompose during carbonization, such as polystyrene latex (PSL), is a promising alternative [10-14]. Synthesis of submicron-sized hollow and porous silica (SiO_2) particles via an aerosol process has been demonstrated by self-assembly of PSL (as the template) and colloidal SiO_2 nanoparticles (NPs) (as the host material) [15-17]. By adjusting the zeta potential and concentration of the PSL NPs, submicron SiO_2 particles containing ordered pores with a close-packed hexagonal arrangement could be

obtained. However, this strategy may not be easily applied to synthesize well-structured hollow or porous carbon particles, because the host carbon NPs are generally hydrophobic in natures which are not compatible with PSL NPs to make a homogeneous mixture. Hence, it is highly required to find an alternative carbon source.

Here, we develop a self-organized dual polymer system to address this issue. Phenolic resin was selected as the carbon source since it contains OH^- groups that may allow control over self-organization with PSL NPs through electrostatic interaction. The electrostatic interaction between phenolic resin and PSL can be tuned by adjusting the sign and magnitude of zeta potential (ζ) of PSL. This is the first report of the use of electrostatic forces to promote the self-organization of polymers within a droplet. Formation mechanisms were evaluated by investigating the electrostatic forces between the two polymers during cross-linking and curing.

3.2. Experiment

Aqueous precursor solution containing phenolic resin (Sumitomo Bakelite Co., Ltd., Japan) and electrically charged PSL beads (~230 nm diameter) were used to prepare spherical carbon nanostructures using a spray pyrolysis by a reported method [10]. Droplets were generated by an ultrasonic nebulizer (1.7 MHz, NE-U17, Omron Healthcare Co., Ltd., Japan) and sprayed through a tubular furnace with four stacked temperature zones set to 150, 300, 700, and 700 °C, as outlined in Scheme 1. N_2 gas (0.8 L min^{-1}) was used to carry the droplets through the furnace. Positively and negatively charged PSL were used to control the self-assembly of phenolic resin. The mass ratio of phenolic resin to PSL was fixed at 0.625.

Characterization. Particle morphology was observed using scanning electron microscopy (SEM, S-5000, 20 kV, Hitachi High-Tech. Corp., Japan) and transmission electron microscopy (TEM) and electron tomography (JEM-2010, 200 kV, JEOL Ltd., Japan). The adsorption capacity of carbon dioxide was profiled by temperature-programed desorption (TPD, BELCAT-A, BEL Japan, Inc., Japan).

Scheme 1. Schematic of the experimental procedure.

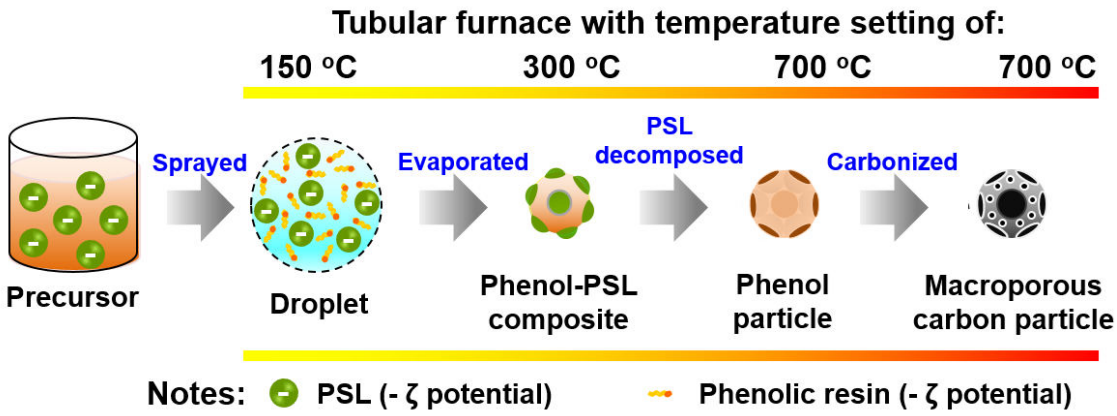

3.3. Results and Discussions

To evaluate the electrostatic interaction between phenolic resin and PSL, the zeta potential of PSL is an important parameter to consider. For positively charged PSL, zeta potential could be controlled by adjusting the quantity of initiator, i.e., 2,2'-azobis (isobutyramidine) dihydrochloride (AIBA). Figure 1(a) indicates that the zeta potential is proportional to AIBA concentration, and is saturated at 3 wt.% and higher. For negatively charged PSL, potassium persulfate was used as an initiator.

The effect of PSL addition on particle morphology was observed by SEM and TEM. In this work, we have defined the morphology of particles into two types as

follows; particles with the observed macropores on the surface are called porous particle, while particles having a macropores covered by complete shell are called hollow particles. Spray pyrolysis of the phenolic resin precursor resulted in spherical particles which are likely microporous, as shown in Figure 1(b) and supporting information, SI 1(a). However, hollow carbon particles were obtained when highly positively charged PSL (ζ = 53 mV) was added (Figure 1(c)). The structure of carbon particles gradually changes from hollow to porous when zeta potential decreases since the electrostatic interaction becomes weaker (Figures 1(d)-(f)). For instance, instead of hollow particles, highly porous carbon particles were achieved when PSL with a zeta potential of 12 mV was used as clearly observed in Figure 1(f). Conversely, addition of negatively charged PSL produces a completely macroporous carbon, as depicted in Figure 1(g). To clearly investigate the inner structure of the carbon particles, TEM analysis of carbon prepared using highly positively charged PSL (ζ = 53 mV) and negatively charged PSL (ζ = -59 mV) was carried out. A clear difference between the structures of two particles could be easily identified from their corresponding TEM images (Figures 1(h)-(i)). The high-resolution (HR)-TEM image in Figure 1(h) shows macropores covered by a thin carbon shell (~5 nm), which confirms the hollow morphology. Surface occupied by macropores can be clearly seen from Figure 1(i) (left), and a triangle-like carbon shell was observed in the HR-TEM image in Figure 1(i) (right), indicating that no coating was formed; the phenol filled only the voids between PSL particles. TEM images of both the hollow and porous carbon samples revealed that the carbon surfaces were decorated with mesopores generated by the release of gas during PSL decomposition and carbonization of the phenolic resin [18].

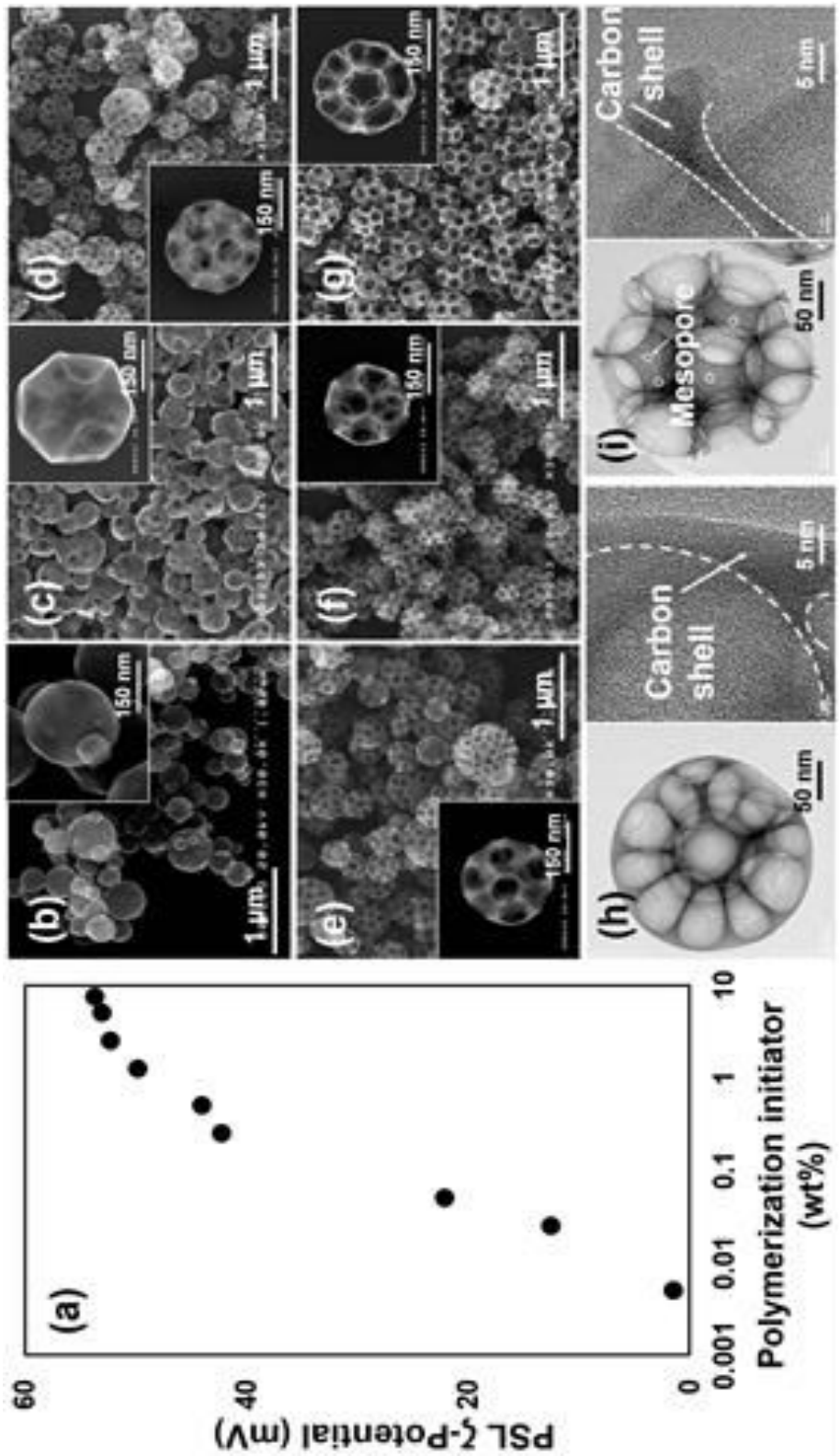

Fig. 3.1. (a) The effect of AIBA concentration on zeta potential of PSL. SEM images of carbon particles prepared (b) without a template, and prepared using a template with a zeta potential of (c) 53 mV, (d) 40 mV, (e) 22 mV, (f) 12 mV, and (g) -59 mV. TEM images of carbon particles prepared using a template with a zeta potential of (h) 53 mV and (i) -59 mV.

Figure 2 shows a proposed model for the formation of nanostructured carbon from phenolic resin. Please note that the temperature of droplets is usually lower than the set-point temperature due to the fast heating process in spray pyrolysis, which could not be analyzed easily due to the paucity of quantitative data. As a consequence, cross-linking and curing processes were not individually examined in this work. The self-assembly of phenolic resin precursor is illustrated in Figure 2(a). In the low temperature zone, a droplet containing oligomers of the phenolic resin is compacted into a spherical cross-linked phenol as water evaporates [6]. A three-dimensional interconnected network is formed between the phenol oligomer units to give microporous spherical carbon particles. The micropores were generated by the release of gas during carbonization of the phenolic resin (SI 1) [18]. Phenolic resin derived carbon particles is naturally contain micropores in its whole surface as reported elsewhere [18]. They were generated by the release of gas during carbonization of phenolic resin. Even though the micropores might be difficult to be clearly observed, but it can be depicted from Figure SI 1(a). To evaluate the structure evolution of carbon particles derived from phenolic resin with and without the addition of polystyrene latex (PSL), thermal behaviors of the phenolic resin, PSL, and phenolic resin-PSL composite were examined at the temperature of 20-800 ^{o}C under a nitrogen atmosphere as shown in Figure SI 1(b). The TGA curve of phenolic resin confirmed the gasses formation during carbonization. The curve exhibit four major stages, in which, the first 3 stages were up to 600 ^{o}C and showed the enormous degradation of ca. ~40%. In this area polymerization of phenol oligomer was occurred, and the weight loss during this heat treatment is ascribed for the release of various gases (CO, CO_2, CH_4, and H_2) and H_2O evaporation depending on the decomposition state of phenolic resin. The last stage,

above 600 ^{o}C represents after carbonization process, in this last stage the weight of sample was relatively stable and only slight degradation was occurred, because carbonization has already achieved. The TGA curve of PSL shows sharp weight loss at 350 ^{o}C and the PSL were completely decomposed at 400 ^{o}C.

TGA curves of the phenolic resin-PSL composites shows similar initial stage of weight loss as phenolic resin. However, sharp weight loss was observed in the range of 400-450 ^{o}C, indicating rapid PSL decomposition. A very small decomposition was then presented at 450-600 ^{o}C and the weight become stable at the above temperature, showing the complete carbonization. The large shift of the decomposition temperature of PSL in phenolic resin-PSL composite toward higher temperature (ΔT ~50 °C) compared to that of pure PSL particle, indicates the composite formation of phenolic resin and PSL. The interaction between phenolic resin and PSL determine the structurization of carbon particles.

Figure 2(b) shows the self-assembly of phenolic resin with positively charged PSL. Phenolic resin in oligomeric form contains OH^- groups and has a zeta potential of -40 mV. Highly positively charged PSL (53 mV) is strongly attracted by the OH^- groups of the phenol oligomers, so that phenolic resin will stick closely to PSL NPs. The individual PSL NPs will be tightened up into the center of droplet. These oligomers then cross-link and cure as water evaporates, leaving phenolic resin-coated PSL. Polymerization of these phenol oligomers is complete before PSL decomposes at a higher temperature, as indicated previously by thermogravimetric analysis [10]. Hollow particles were formed when the quantity of highly positively charged PSL NPs is small enough to be covered by phenolic resin and the excess phenolic resin serves as a shell. Porous particles may form as well if no enough phenolic resin is available to form a

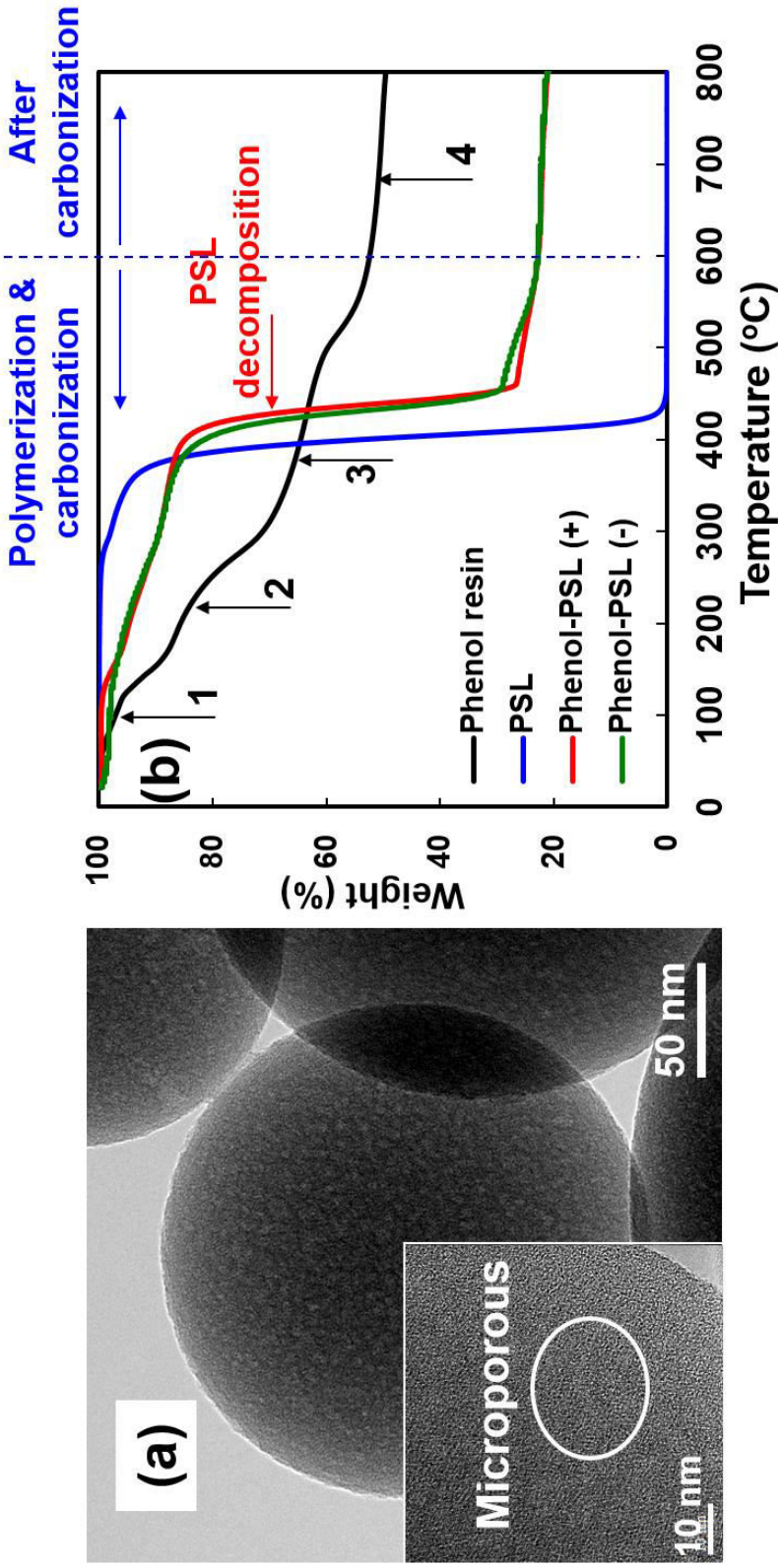

Fig. 3. SI. 1. (a) TEM and HR-TEM images of microporous carbon particles and (b) TGA thermogram of the phenolic resin, PSL, and phenolic resin-PSL composite.

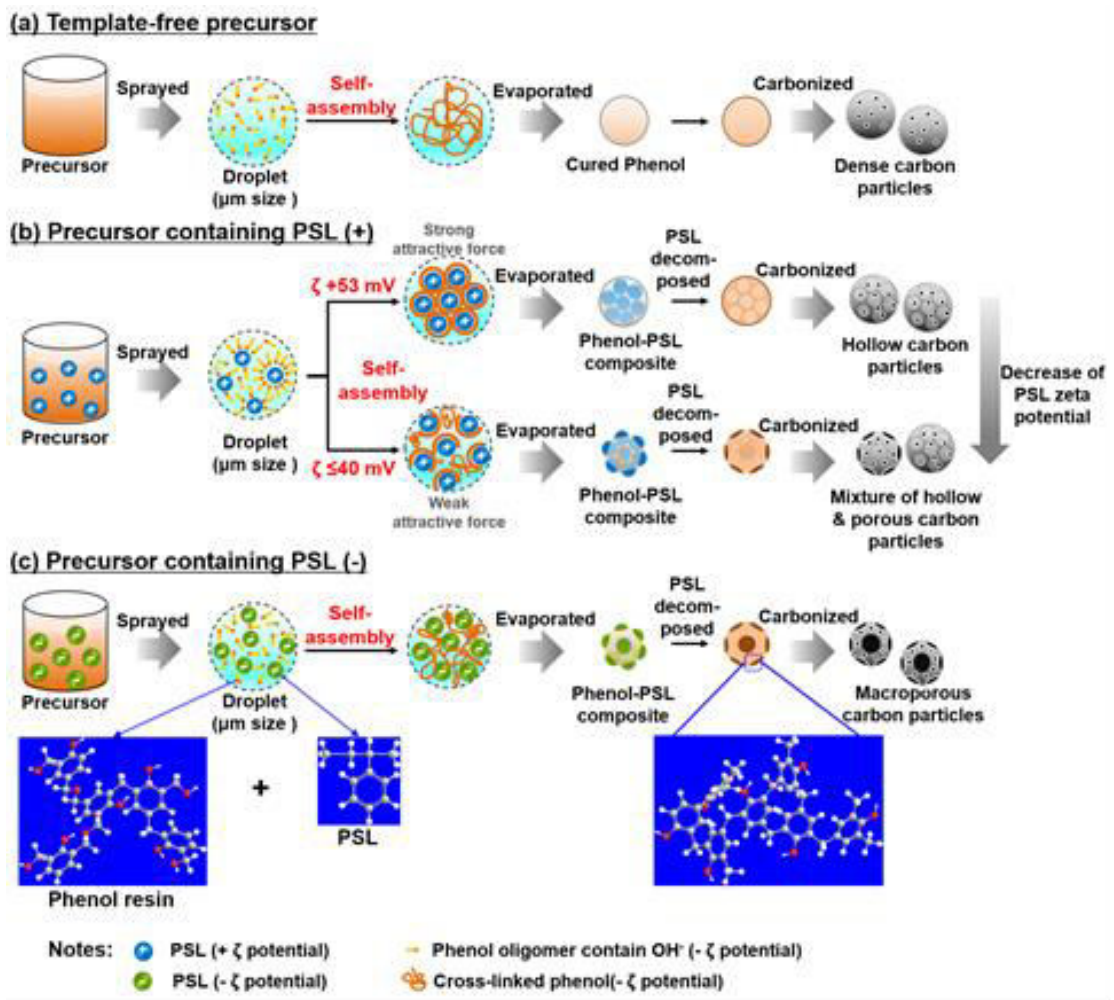

Fig. 3.2. Schematic diagram of nanostructured particle formation during spray pyrolysis from each precursor: (a) phenolic resin, (b) phenolic resin and positively charged PSL, and (c) phenolic resin and negatively charged PSL.

shell. Most of phenolic resin fills the voids between PSL NPs, which are randomly distributed inside the droplet when the electrostatic attraction force becomes weaker ($\zeta \leq 40$ mV). Here, more porous particles are formed after PSL decomposition since the phenolic resin is also uniformly distributed without formation of a shell structure. This is also very similar to the case of negatively charged PSL NPs addition, where the PSL NPs are kept separately from each other, evenly distributed inside the droplet, as shown in Figure 2(c).

The above formation pathways are proved by our careful SEM and TEM analyses. PSL particles naturally form a hexagonal arrangement because of their high monodispersity, as shown in Figure 3(a,b). When an attractive force is applied, PSL is coated by phenolic resin. The resulting carbon particles possess compact, regular polyhedral structures, as depicted in the inset of Figure 3(a). In contrast, porous carbon particles have spherical structures, although the pores are hexagonally arranged, as shown in the inset of Figure 3(b). This phenomenon arises from the repulsive force that exists between PSL and phenol until the water completely evaporates from the droplet and polymerization occurs.

The morphology of the carbon particles was also determined by the quantity of PSL contained in a droplet. Each sprayed droplet may contain different amounts of PSL, and we observed carbon particles with various morphologies that depended on the amount of PSL were found, as shown in Figure 3(c). The changes in particle morphology are similar to those reported previously [17,19]. The particle size was also influenced by the amount of PSL. The 2D correlation between carbon particle radius, *R*, and PSL radius, *r*, as derived from trigonometry rules are as follows:

$$R = r \quad \text{for} \quad n = 1; \tag{1.a}$$

$$R = 2r \quad \text{for} \quad n = 2; \tag{1.b}$$

$$R = 1 + \frac{2}{3}\sqrt{3} \div r \quad \text{for} \quad n = 3; \tag{1.c}$$

$$R = \left(1 + \sqrt{2}\right) r \quad \text{for} \quad n = 4; \tag{1.d}$$

$$R = 2.7r \quad \text{for} \quad n = 5; \tag{1.e}$$

$$R = 3r \quad \text{for} \quad n = 6. \tag{1.f}$$

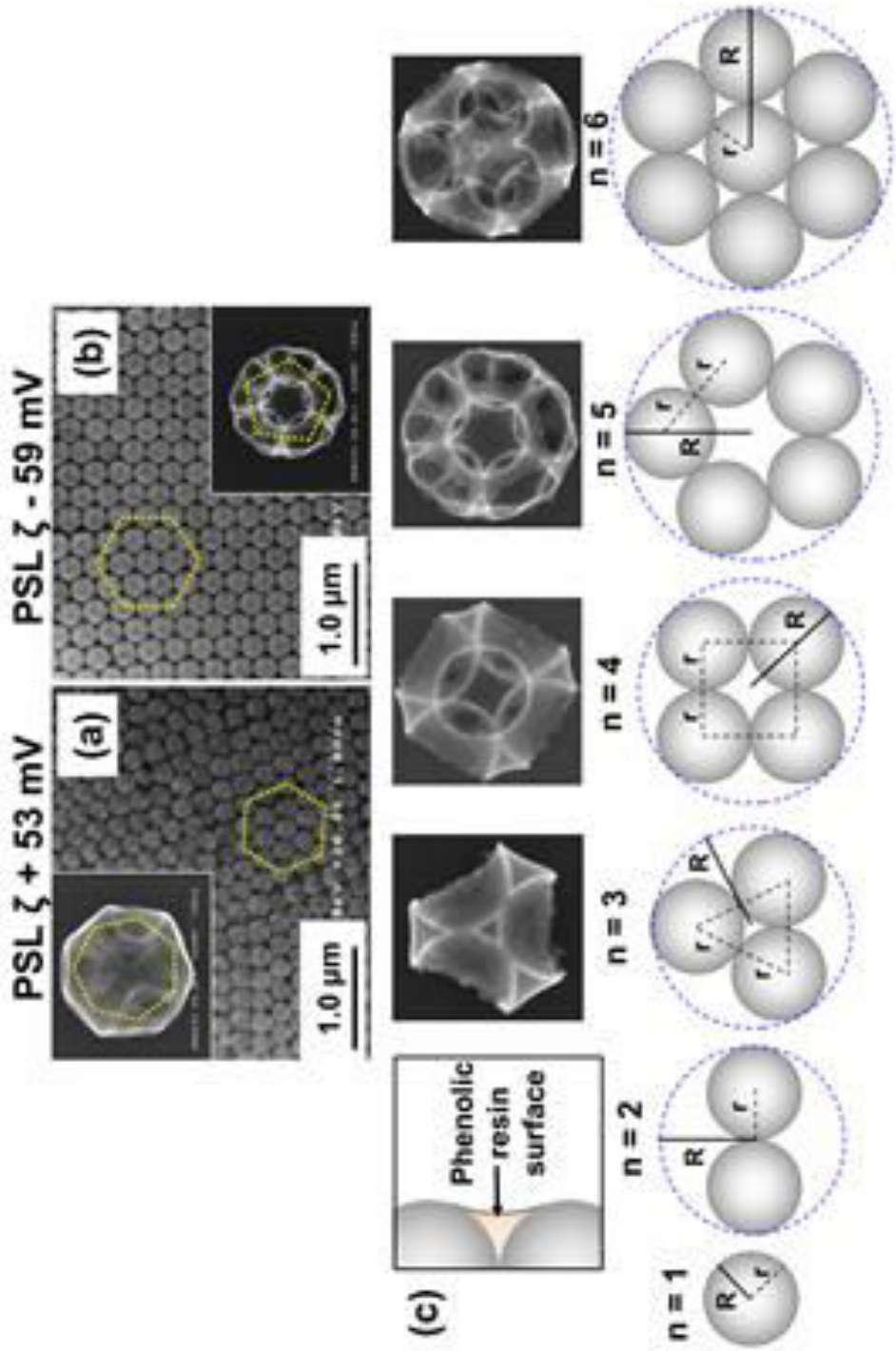

Fig. 3.3. SEM images of (a) PSL (ζ = 53 mV) and (b) PSL (ζ = -59 mV). The insets show the obtained carbon particles. (c) Model of PSL arrangement in a droplet.

To analyze the formation of a carbon shell more accurately, samples were investigated by electron tomography (SI 2). ET images of the hollow and porous carbons are shown in Figure SI 2(a) and (b), respectively. The red, green, and blue axes represent the *x*-, *y*-, and *z*- axes, respectively. A slice of the ET image taken at $z = r$ (r is the radius of the observed sample) is shown in the 3rd image of Figure SI 2 (a and b). The ET slice image in Figure SI 2 (a) shows that the carbon is hollow with a thin carbon shell. This confirms that the PSL is covered by a layer of phenol oligomer, and it is strongly attracted to the surface of the PSL. Figure SI 2 (b) shows highly porous carbon and macropores with an interconnected system. The hollow morphology with a thin carbon shell and porous morphology with an interconnected system of macropores were confirmed for different samples, and found consistent with the SEM observations.

The CO_2 adsorption characteristics of prepared hollow and porous carbon particles were investigated by temperature programmed desorption of CO_2 at 50 –500 °C, and 1 bar, with heating rate of 5 ^{o}C min^{-1}. Two major desorption peaks were observed for both types of particles, at 120 and 280 °C, respectively (SI 3). The adsorbed CO_2 was 3.04 and 4.78 mmol g^{-1} for hollow and porous carbon particles, respectively, which were categorized as a high performance as can be seen from the comparison of CO_2 adsorption capacities with other materials as summarized in Table SI 1 [21,22]. Porous carbon shows higher activity than hollow carbon due to its increased active area as compared to its hollow counterpart. This result also reveals that porous carbon derived from phenol is more likely to be applied as a CO_2 adsorbent and in-storage. It is similar to the results of CeO_2 nanocrystal catalyst analysis where the adsorption performance was highly dependent on the particles morphology.

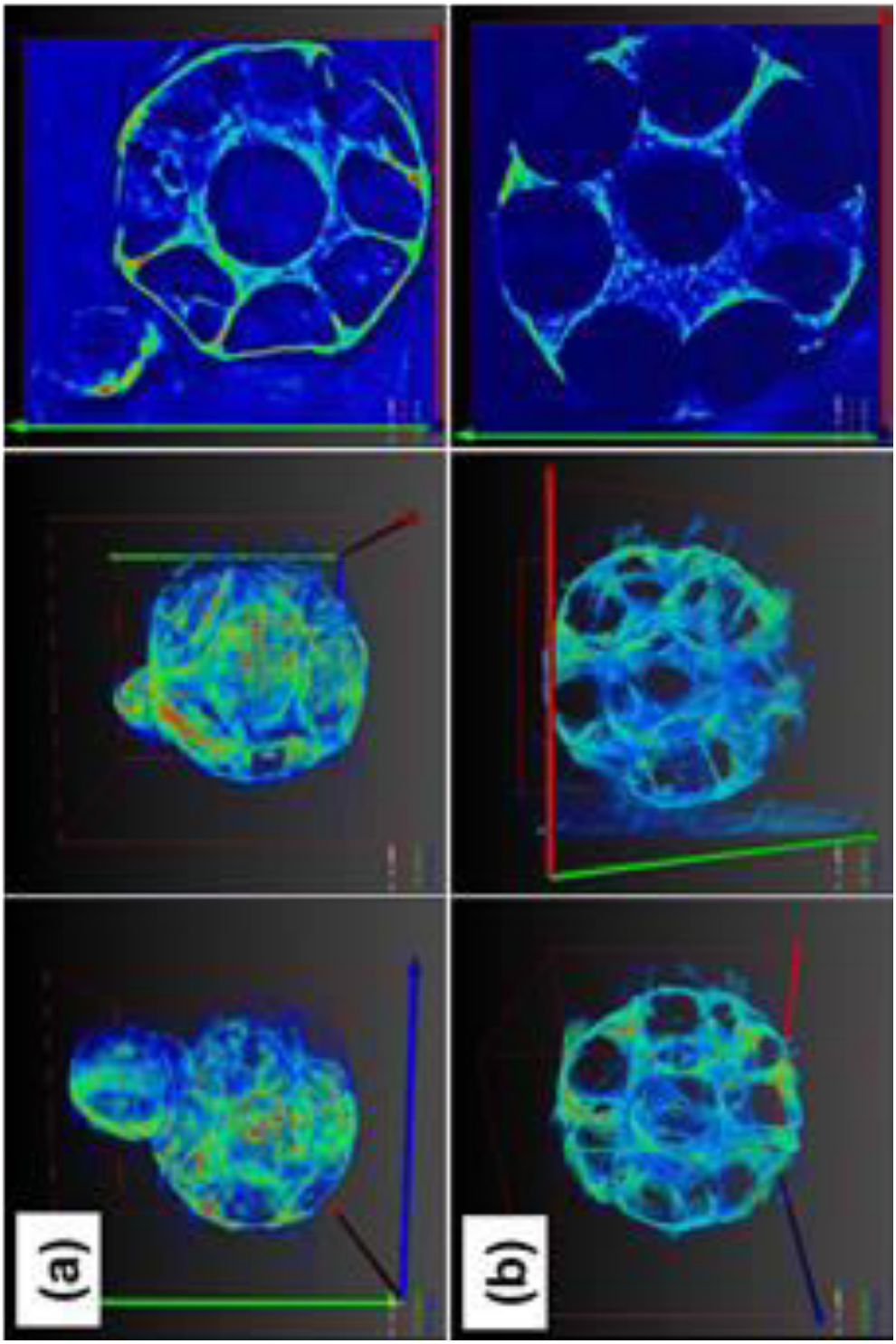

Fig. 3. SI. 2. Electron tomography (ET) images of: (a) hollow and (b) porous carbon particles.

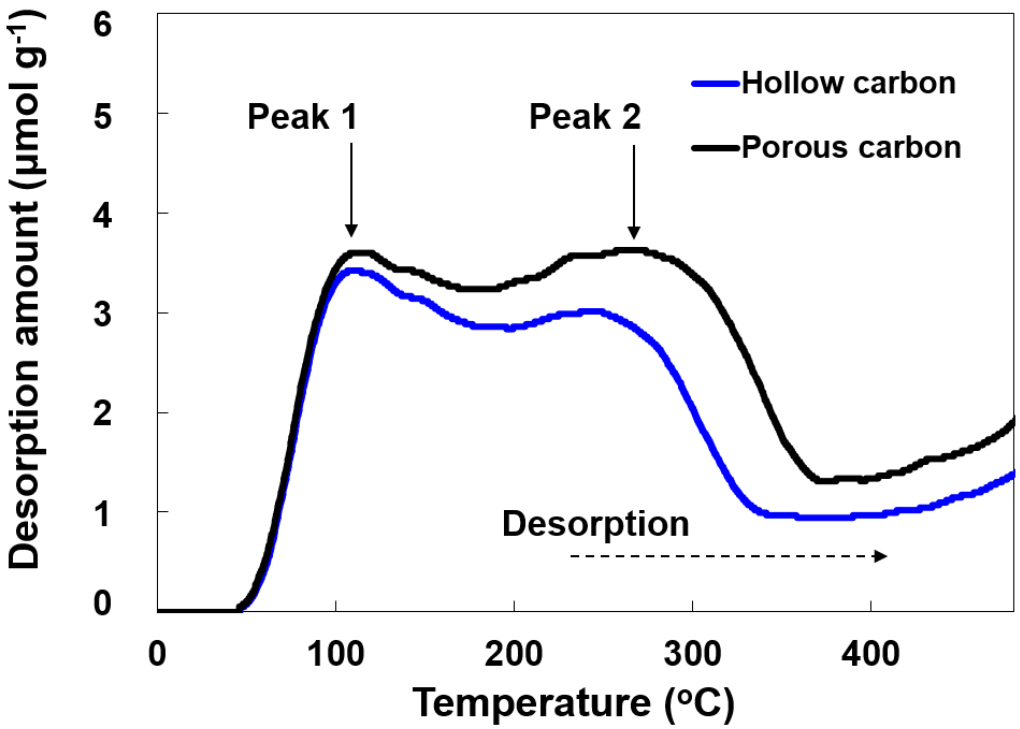

Fig. 3. SI. 3. CO_2 TPD profile of hollow and porous carbon particles.

Surface functional group on the prepared porous carbon particles was examine to determine the limit of prepared carbon particles performance as shown as FT-IR curve (SI 4). Since both of porous and hollow carbon particles were prepared from the same source, it is believed that the contained functional groups are similar, which proven by similar IR spectrum of mesoporous carbon particles from phenolic resin shown elsewhere [18]. FT-IR spectrum in Figure SI 4 shows a weak broad peak at 3350 cm^{-1} indicating the presence of hydrogen bonds such as OH···OH, OH···O (ether oxygen), or OH···O=C on the surface. An aromatic bond from benzene was indicated by a weak peak at 3070 cm^{-1}. An aromatic ring C=C bond was also presented at 1600 cm^{-1}. A strong peak at 1320 cm^{-1} that corresponds to a C-O stretching vibration was observed for the carbonized sample.

Table 3. SI. 1. CO_2 TPD profile of hollow and porous carbon particles.

Sample	Material	CO_2 adsorption capacity (mmol g^{-1})	Source
IBN9-NC1	N-dope carbon	1.81	Zhao, Y., et al.[20]
IBN9-NC1-A	Activated N-dope carbon using KOH	4.50	
CeO_2 spindles	Ceria nanocrystal	0.73	Wang, S., et al.[21]
CeO_2 rods	Ceria nanocrystal	0.74	
CeO_2 cubes	Ceria nanocrystal	0.44	
CeO_2 octahedrons	Ceria nanocrystal	0.15	
Hollow carbon	Carbon	3.04	Balgis, R., et al. (current work)
Porous carbon	Carbon	4.78	

The C-O stretching vibration (1320 cm^{-1}) observed from the spectrum suggests that higher temperature of spray pyrolysis may be needed to obtain oxygen-free carbon particles. It gives us an overview that better performance of CO_2 adsorption may be obtained from oxygen-free carbon particles prepared by optimizing the experimental condition. Porous carbon shows higher activity than hollow carbon due to its increased active area. The preliminary results implicate carbon particles derived from phenolic resin are promising to be applied as a CO_2 adsorbent and in-storage. The effect of functional groups and particle morphology on the adsorption capacity are only a working hypothesis now. Nevertheless, the possibility of achieving nanostructured hollow and porous carbon particles through electrostatically self-organized dual polymer system is exciting. It is hoped that with continuing work on the examining experimental conditions of spray pyrolysis system and understanding the physical and chemical properties of particles, such as specific surface area, Raman spectra and TG-MS, carbon particles as a high performance gas adsorbent may be prepared.

3.4. Conclusions and outlook

Artistic hollow and porous carbon particles were prepared by spray pyrolysis of a dual polymer system. The morphology of the prepared particles can be well tailored by precisely tuning the attractive or repulsive force in a droplet. Hollow carbon particles were formed due to the strong attractive force between phenolic resin and highly positively charged PSL. Porous carbon particles were obtain when the attractive force was weaken or when repulsive force was occur due to the presence of negatively charged PSL. The as-prepared particles readily adsorb CO_2 because they contain various aromatic groups derived from the phenolic resin and large active areas. This study opens

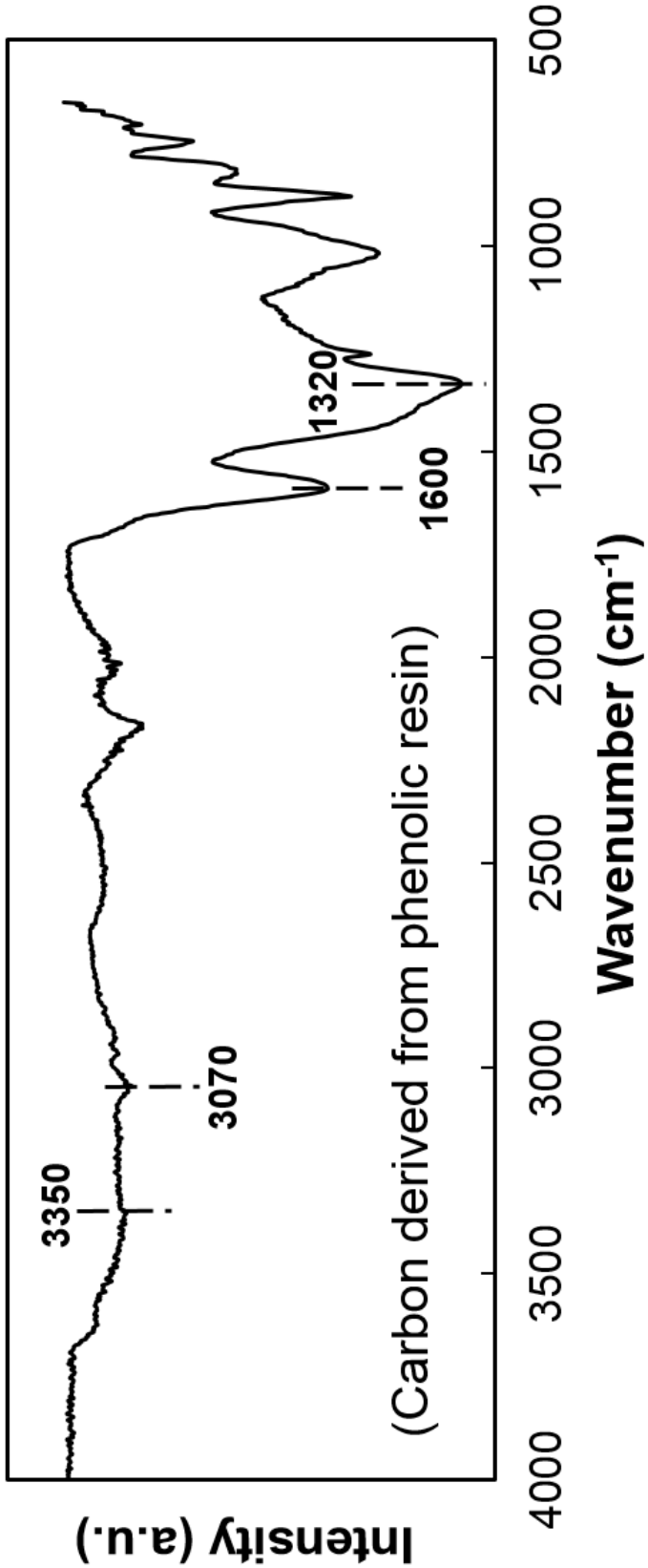

Fig. 3. SI. 4. FT-IR spectrum of porous carbon particles.

a new opportunity for the development of advanced adsorbent material for the future needs. The detail experimental conditions of spray pyrolysis system and the properties of carbon particles are still being investigated and will be reported in the near future.

3.5. References

[1] C. Wang, Y. Wang, J. Graser, R. Zhao, F. Gao, M. J. O'Connell, ACS Nano 7, 11156 (2013).

[2] Z.-A. Qiao, B. Guo, A. J. Binder, J. Chen, G. M. Veith, S. Dai, Nano Lett 13, 207 (2013).

[3] C.-M. Yang, H. Noguchi, K. Murata, M. Yudasaka, A. Hashimoto, S. Iijima, K. Kaneko, Adv. Mater. 17, 866 (2005).

[4] J. Liu, T. Yang, D.-W. Wang, G. Q. (Max) Lu, D. Zhao, S. Z. Qiao, Nat. Comm. 4, 1 (2013).

[5] C. Boissiere, D. Grosso, A. Chaumonnot, L. Nicole, C. Sanchez, Adv. Mater. 23, 599 (2011).

[6] X. Yu, S. Ding, Z. Meng, J. Liu, X. Qu, Y. Lu, Z. Yang, Colloid Polym. Sci. 286, 1361 (2008).

[7] J. Schuster, G. He, B. Mandlmeier, T. Yim, K. T. Lee, T. Bein, L. F. Nazar, Angew. Chem., Int. Ed. 51, 3591 (2012).

[8] R. Ryoo, S. H. Joo, S. Jun, J. Phys. Chem. B 103, 7743 (1999).

[9] I. Muylaert, A. Verberckmoes, J. De Decker, P. Van Der Voort, Adv. Colloid Interface Sci. 175, 39 (2012).

[10] R. Balgis, S. Sago, G. M. Anilkumar, T. Ogi, K. Okuyama, ACS Appl. Mater. Interfaces 5, 11944 (2013).

[11] Y. N. Ko, S. B. Park, K. Y. Jung, Y. C. Kang, Nano Lett. 13, 5462 (2013).

[12] D. Y. Zhao, Q. S. Huo, J. L. Feng, B. F. Chmelka, G. D. Stucky, J. Am. Chem. Soc. 120, 6024 (1998).

[13] C. T. Kresge, M. E. Leonowicz, W. J. Roth, J. C. Vartuli J. S. Beck, Nature 359, 710 (1992).

[14] A. Thomas, Angew. Chem., Int. Ed. 49, 8328 (2010).

[15] F. Iskandar, Mikrajuddin, K. Okuyama, Nano Lett. 2, 389 (2002).

[16] R. Balgis, G. M. Anilkumar, S. Sago, T. Ogi, K. Okuyama, J. Power Sources 229, 58 (2013).

[17] S. Y. Lee, L. Gradon, S. Janeczko, F. Iskandar, K. Okuyama, ACS Nano 4, 4717 (2010).

[18] Y. J. Kim, M. I. Kim, C. H. Yun, J. Y. Chang, C. R. Park, M. Inagaki, J. Colloid Interface Sci. 274, 555 (2004).

[19] D. V. Talapin, E. V. Schevchenko, M. I. Bodnarchuk, X. Ye, J. Chen, C. B. Murray, Nature 461, 964 (2009).

[20] Y. Zhao, L. Zhao, K. X. Yao, Y. Yang, Q. Zhang, Y. Han, J. Mater. Chem. 22, 19726 (2012).

[21] S. Wang, L. Zhao, W. Wang, Y. Zhao, G. Zhang, X. Ma, J. Gong, Nanoscale 5, 5582 (2013).

Chapter 4

Electrospun Pt/SnO_2 nanofibers as an excellent electrocatalysts for hydrogen oxidation reaction with ORR-blocking characteristic

4.1. Introduction

Polymer electrolyte membrane fuel cells (PEMFCs) are of great scientific interest as future energy sources owing to their advantages such as high energy conversion efficiency, a wide operation temperature, and low/zero emissions [1-3]. A couple of reactions are necessary to continuously generate electric current during the operations of PEMFCs: a hydrogen oxidation reaction (HOR) at the anode, and an oxygen reduction reaction (ORR) at the cathode. Platinum-based nanoparticles supported on high surface area carbon are widely used to catalyze both HOR and ORR [1,2]. Research on electrocatalyst materials has been focused on cathode ORR catalyst development due to sluggish reactions that result in a voltage drop in fuel cells. However, over-potential at the anode during shutdown and startup causes an undesired ORR and significantly contributes to an overall fuel cell voltage drop. Therefore, a design of electrocatalyst materials that tolerant to an ORR without sacrificing HOR activity is extremely challenging [4-6]. Prior study has shown that the surface modification of Pt by an organic molecules effectively block an ORR [4,5]. However, the HOR activity of modified Pt catalyst was sacrificed.

Pt nanoparticles dispersed on the metal oxide support materials are considered to be an effective strategy to increase the activity and the stability of electrocatalyst

[7,8]. Presumably, a strong interaction between Pt and a metal oxide could result in unique properties, including ORR-blocking. In recent years, various metal oxides have been investigated as catalyst support materials [7,8]. Among these oxides, SnO_2 is very promising due to its characteristics such as a high electron mobility, reasonable electric conductivity, and corrosion resistance [9-11]. Previous studies have reported that Pt nanoparticles grown *ex situ* on the surface of SnO_2 via an impregnation method exhibited significant tolerance against potential cycling of up to 10000 cycles [9]. However, the HOR activity in Pt/SnO_2 with tolerance to ORR activity has never been elucidated, and its electrocatalytic activity remains unsatisfactory.

The structural engineering of Pt/SnO_2 into nanofiber morphology would enhance the performance of PEMFCs, due to the fact that nanofiber morphology provides an easy access to electron transport along an alignment that is contrary to that of nanoparticles where there is a significant interface between particles that may add resistance to the system [12]. Herein, we present a novel *in situ* method to grow Pt nanoparticles on SnO_2 nanofiber matrix via electrospinning. The processing technique and the electrochemical activities are reported herein.

4.2. Experiment

Raw materials used in the experiment were polyacrylonitrile (PAN, M_W = 150000 gr/mol, Sigma Aldrich, USA), tin chloride pentahydrate ($SnCl_4.5H_2O$, Nacalai Tesque, Japan) hexachloroplatinic acid ($H_2PtCl_6.6H_2O$, Mitsuwa Chemical, Japan), and *N,N*-dimethylformamide (C_3H_7NO, DMF, Sigma Aldrich, USA). SnO_2 and Pt/SnO_2 nanofibers were synthesized in order to investigate the effect of Pt deposition on SnO_2 nanofibers to the electrocatalytic activity. A precursor containing of PAN (1.422 g),

$SnCl_4.5H_2O$ (1 g), and DMF (12.8 g) was electrospun to produce SnO_2 nanofibers. In another experiment, $H_2PtCl_6.6H_2O$ (0.05 g) was added to produce Pt/SnO_2 nanofibers. The general setup for electrospinning was similar to that of previously reported work [13]. The voltage, distance between needle and electrode, precursor flow rate, and rotation drum velocity were 14 kV, 23 cm, 20 μl/min, and 450 rpm, respectively. The electrospun composite nanofibers were then heated at 500 ^oC at a heating rate of 2 ^oC/min for 4 h under an ambient air atmosphere.

The morphology of nanofibers was examined using a transmission electron microscope (TEM; Topcon EM-002BF) and a field emission scanning electron microscope (FE-SEM; Hitachi S-5000). The crystalline structures were examined using X-ray diffraction (XRD) measurement (Rigaku RINT2000 X-ray diffractometer with nickel filtered Cu-K_α (λ=0.154 nm) radiation at 40 kV and 30 mA with a scanning rate of 0.02^o/2θ). Inductively coupled plasma measurement (ICP, SII, S6000) was applied to determine the amount of Pt loading on the Pt/SnO_2 nanofibers.

A potentiostat (Hokuto Denko, HR-301) was used for electrochemical measurement. Catalyst inks were prepared following a procedure reported previously [2]. A known amount of catalyst was mixed with 6 mL isopropanol (Cica-reagent, Kanto Chemical Co. Inc., Japan) and 19 mL ultrapure water, followed by the addition of 100 μL of a Nafion® dispersion solution (5 wt.%, Wako Pure Chemical Industries, Ltd., Japan). The catalyst ink was then placed in an ice bath and ultrasonicated for 30 min. For the electrode preparation, 10 μL of catalyst ink contained 3.39 μg of Pt, was transferred onto the polished glassy carbon disk (area 0.196 cm^2) and dried to produce a thin film of the catalyst layer. The measurement setup was a typical three-electrode system, which consisted of a working electrode, a Pt wire as the counter electrode, and a

reversible hydrogen electrode (RHE) as the reference electrode. All measurements were performed at (25±0.5)^{o}C using an aqueous electrolyte solution of 0.1 M $HClO_4$. The electrolyte solution was saturated with nitrogen gas for 30 minutes before cyclic voltammetry (CV) measurements. The CV measurements were scanned between 0 and 1.2 V vs. RHE with a sweep rate of 100 mV/s. The HOR activity was measured by linear sweep voltammetry (LSV) method. The saturation gas was switched to hydrogen for 30 minutes prior to LSV measurement. Rotation rate was controlled at 400, 900, 1600, 2500, and 3600 rpm. Measurements were carried out at 10 mVs^{-1} sweep rates and scanned between 0 and 1.2 V vs. RHE. The electrochemical properties of commercial Pt/C catalyst (46 wt.% Pt, purchased from Tanaka Kikinzoku Kogyo, TKK, Japan) were also measured.

4.3. Results and Discussions

The XRD patterns of SnO_2 and Pt/SnO_2 nanofibers are shown in Figure 1. Both diffraction patterns were consistent with references, with no formation of any other crystal phase (e.g., PtO). This observation revealed that Pt nanoparticles can be grown *in situ* simultaneously with metal oxide formation only by heat treatment under an air atmosphere. Presumably, Sn atoms are more attractive than Pt atoms on making a bounding with O atoms during the crystal growth, so that SnO_2 formation was more favorable. The diffraction peaks of SnO_2 and Pt can be indexed to the tetragonal rutile and face-centered cubic (fcc) structure according to the JCPDS Cards Nos. 41-1445 and 04-0802, respectively. The crystallite sizes of SnO_2 were calculated following the Scherer law and were 21.48 and 23.74 nm for SnO_2 and Pt/SnO_2 nanofibers, respectively. Meanwhile, the crystallite size of Pt was calculated to be 19.50 nm for

Pt/SnO$_2$ nanofibers. The optimum size of Pt particles for electrocatalytic activity was reported to be below 5 nm [14]. This fact indicates that the electrocatalytic activity of the present Pt/SnO$_2$ nanofibers might not be optimum. It is a great challenge to reduce the Pt size on Pt/SnO$_2$ nanofibers to below 5 nm under the present processing conditions.

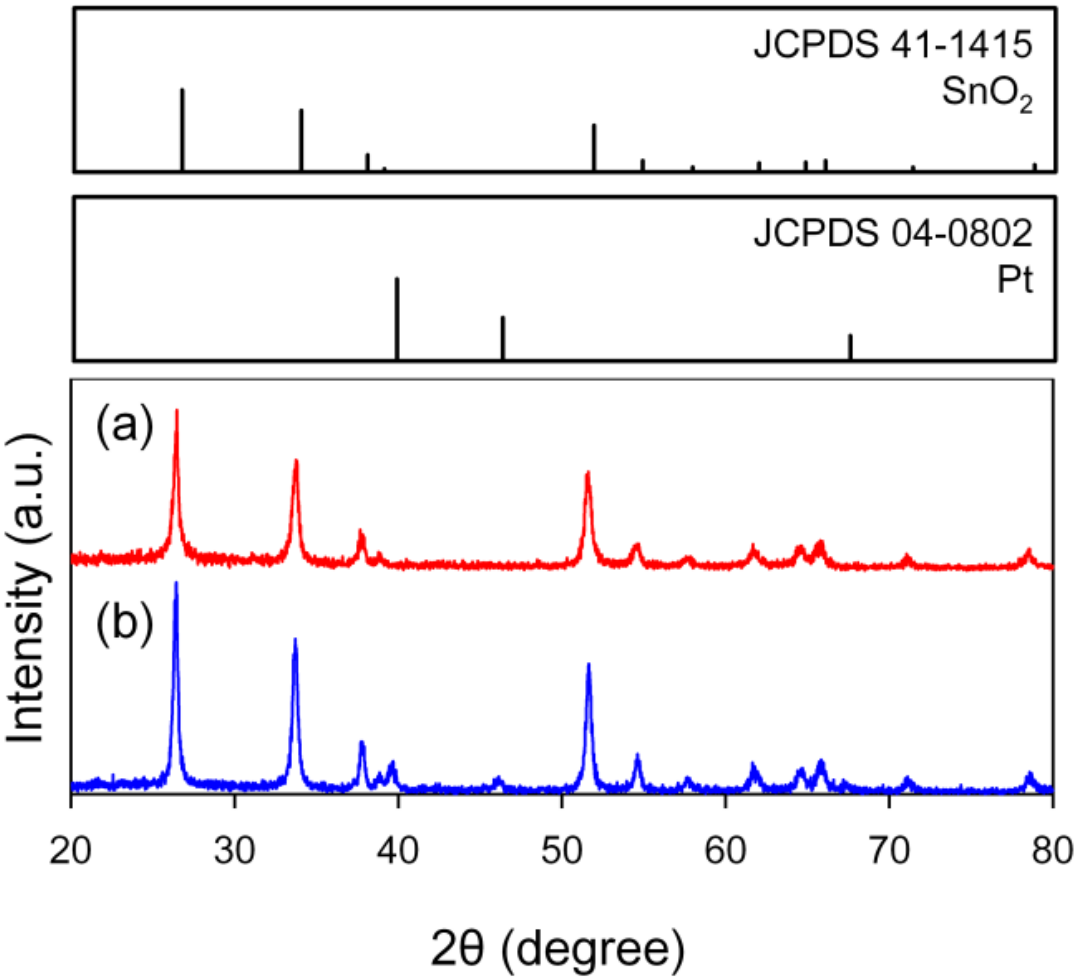

Fig. 4.1. XRD patterns of (a) SnO$_2$ nanofibers and (b) Pt/SnO$_2$ nanofibers.

Figure 2 shows the FE-SEM, TEM, HR-TEM, and elemental mapping of Pt/SnO$_2$ nanofibers. The morphology of SnO$_2$ nanofibers was found similar to that of Pt/SnO$_2$ nanofibers. It was found that the average diameter of prepared nanofibers was

~400 nm. The as-prepared nanofibers were very flexible and smooth with a length up to several centimeters prior to the heat treatment. After calcination, the surface of the nanofibers became rough, porous, and grainy. The lengths of the nanofibers were reduced to several micrometers, as shown in Figure2(a). The existence of Pt nanoparticles on the tin oxide matrix was clearly visible, as shown by TEM and HR-TEM images (Figure 2(b), 2(c)). The actual Pt loading on the prepared Pt/SnO_2 nanofibers was measured as 4.03 wt.% according to the ICP measurement. Elemental mapping of Pt/SnO_2 nanofibers was conducted to verify the elemental composition of the nanofibers (Figure 2(d)). Sn, O and Pt atoms were confirmed as existing to be well-distributed on the nanofiber matrix. In addition, C and N atoms were also detected in the nanofiber. They may derive as a byproduct of polyacrylonitrile.

The cyclic voltammogram, recorded at 200th cycle, are presented in Figure 3(a). The voltammogram are necessary to determine the electrochemically active surface area (ECSA). The CV-curve of Pt/SnO_2 nanofibers was very stable up to 200th cycle (see Supporting Information). SnO_2 nanofibers had a very small ECSA indicated by its CV-curve that almost formed a straight line. On the other hand, the presence of Pt nanoparticles on SnO_2 nanofibers significantly increased the ECSA. Typically, there are three regions in a CV-curve that correspond to hydrogen adsorption-desorption, double-layer charging, and Pt oxidation-reduction activities that could be clearly seen on CV-curve of Pt/C TKK [4,5]. However, the CV-curve of Pt/SnO_2 nanofibers shows a unique characteristic. It shows the features of hydrogen adsorption-desorption at $E < 0.4$ V, however it does not show the Pt oxidation-reduction activity, indicated by its CV-curve that significantly suppressed at $E > 0.6$ V. Based on this phenomenon, we

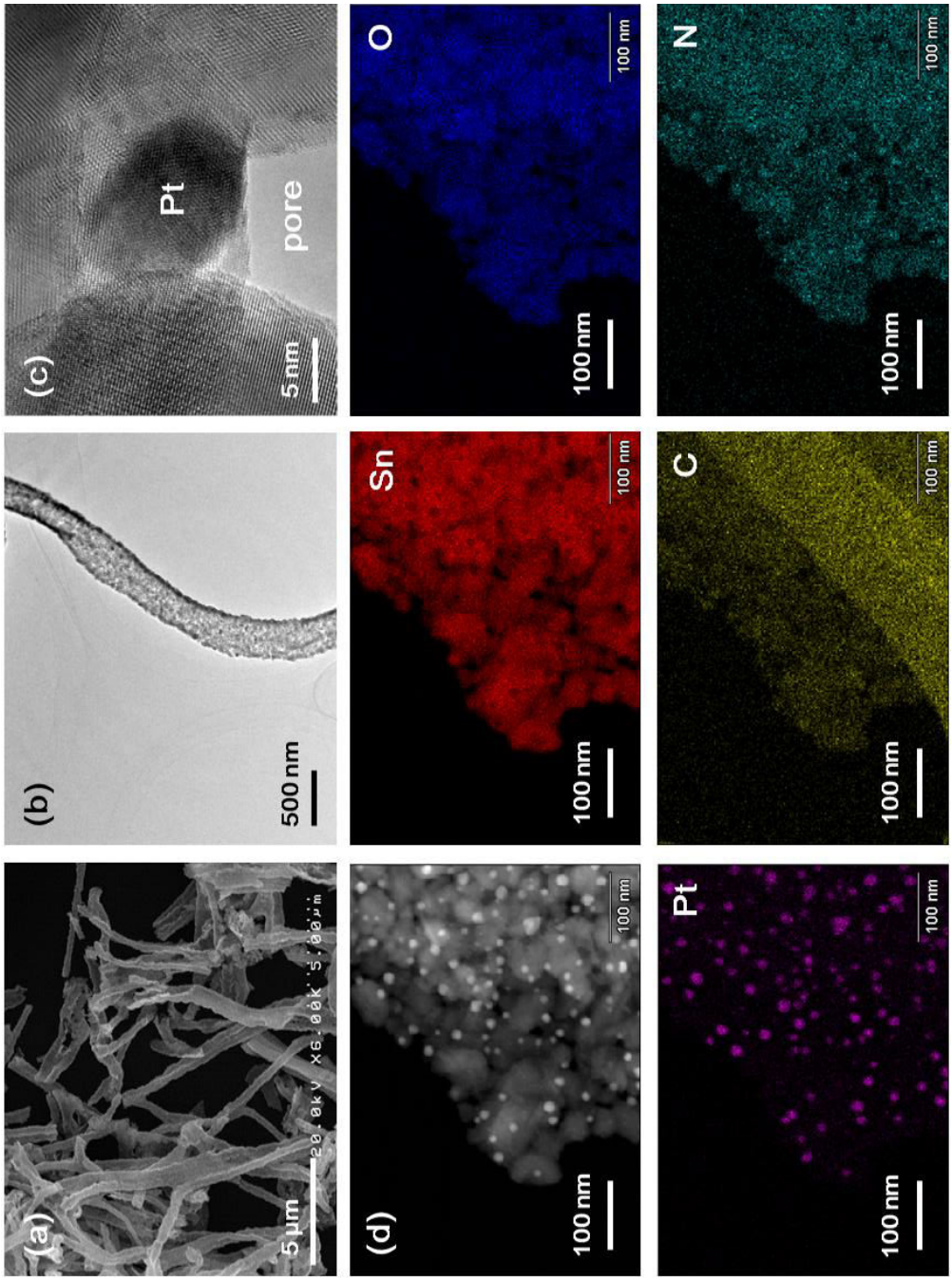

Fig. 4.2. (a) FE-SEM image, (b) TEM image, (c) high-resolution TEM image, and (d) elemental mapping of Pt/SnO_2 nanofibers.

assume that Pt/SnO$_2$ nanofibers had an ORR-blocking characteristic (see Supporting Information). It is a great challenge to develop this kind of electrocatalyst with high ORR activity. The unique activity of prepared Pt/SnO$_2$ nanofibers was probably due to the presence of organic nitrile-group molecules on nanofibers as shown by elemental mapping. Previous study showed that PAN-based nanofibers had nitrile molecules derived from polyacrylonitrile, and this molecules are known to be easily adsorbed by hydroxyl molecules [13,15]. Pt nanoparticles are typical of conductive material for

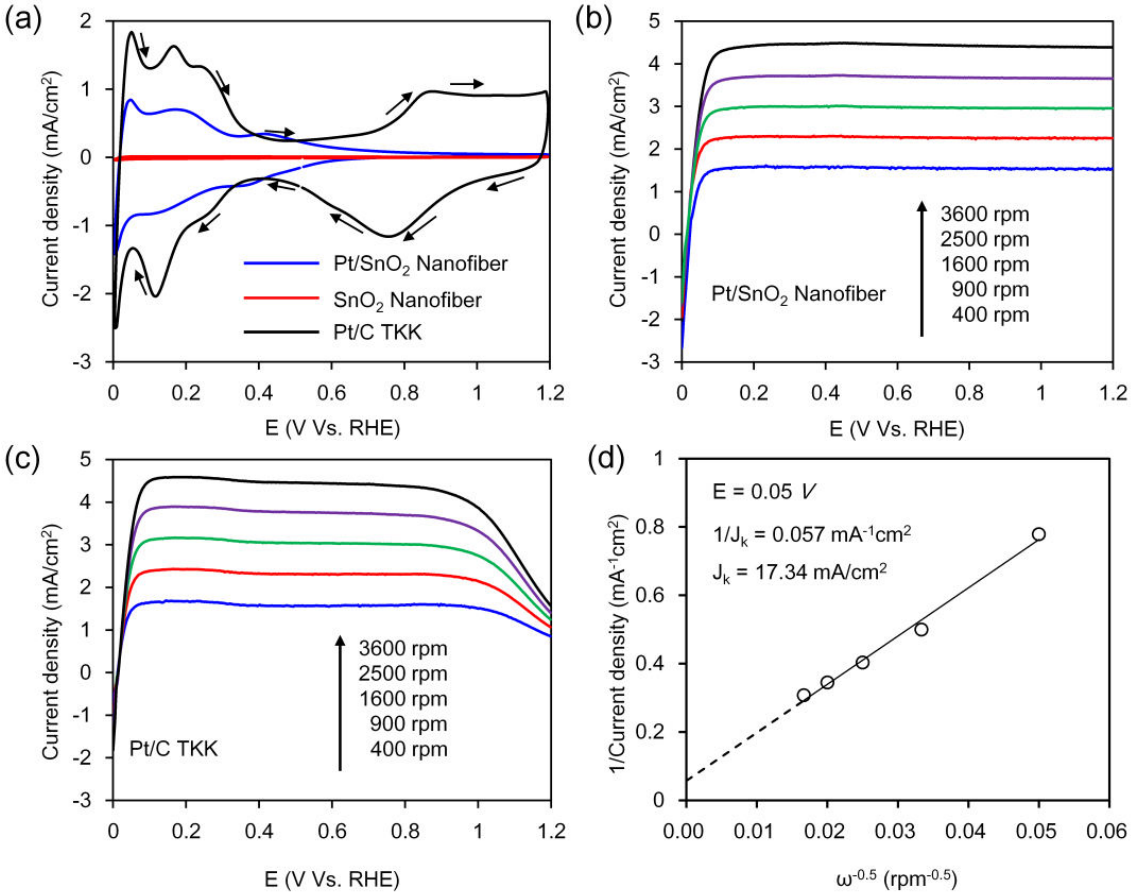

Fig. 4.3. (a) Cyclic voltammogram of SnO$_2$ nanofibers, Pt/SnO$_2$ nanofibers, and Pt/C TKK (b) Linear sweep voltammograms of Pt/SnO$_2$ nanofibers, (c) Linear sweep voltammograms of Pt/C TKK, (d) Kouteky–Levich plot of Pt/SnO$_2$ nanofibers in the diffusion potential region E = 0.05 V.

hydroxyl molecules. It makes hydroxyl molecules easily transferred to near Pt nanoparticles site and finally cover the surface of Pt nanoparticles and introduce nitrile group to the Pt/SnO$_2$ nanofibers simultaneously. It has been shown that high hydroxyl coverage on Pt nanoparticle inhibits ORR activity [16].

The ECSA values were then calculated using the following equation:

$$\text{ECSA} = \frac{Q_H}{Q_0 \times m_{Pt}} = \frac{v^{-1}\int IdE}{Q_0 \times m_{Pt}}, \quad (1)$$

where Q_H is the hydrogen adsorption charge, v is the sweep rate of the CV measurement, I is the measured electric current, E is the electric potential, Q_0 is the charged required for hydrogen adsorption on Pt surface (210 μC), and m_{Pt} is the mass of Pt nanoparticles on the electrode. The ECSA values were 81.17, and 98.54 m^2/g-Pt for Pt/SnO$_2$ nanofibers and Pt/C TKK, respectively. The ECSA of Pt/SnO$_2$ nanofibers was lower than Pt/C TKK. However, the low amount of Pt-loading on Pt/SnO$_2$ nanofibers (4.03 wt %) offers great advantages on the production cost.

The polarization curves of HOR activity for Pt/SnO$_2$ nanofibers and Pt/C TKK are shown in Figure 3(b) and 3(c). The diffusion-limited currents were achieved at a very low potential at 0.07 V for both samples. It was clear that the diffusion-limited current of a Pt/SnO$_2$ nanofiber was very stable even at high potential (E > 0.8 V). On the other hand, the diffusion-limited current of Pt/C TKK was slightly decreased at moderate potential (0.4 V< E <0.8 V) and significantly decreased at high potential (E > 0.8), probably due to double-layer charging effect and to increasing oxidation on Pt surface that contribute for ORR activity [17]. This phenomenon confirmed that Pt/SnO$_2$ nanofibers have an excellent HOR activity. The limiting current density of Pt/SnO$_2$ nanofibers was 3.71 mA/cm^2 at 2500 rpm. A Koutecky-levich plot of Pt/SnO$_2$

nanofibers is shown in Figure 3(d). The value of current density controlled by reactant diffusion determined from the intercept was 17.34 mA/cm^2.

4.4. Conclusions

The present study demonstrated an effective strategy to design an anode catalyst using Pt/SnO_2 nanofibers. Pt nanoparticles were successfully grown *in situ* on the electrospun SnO_2 nanofibers. The Pt/SnO_2 nanofibers showed unique electrocatalytic activity by allowing a hydrogen oxidation reaction while simultaneously inhibits an oxygen reduction reaction. The ECSA of Pt/SnO_2 nanofibers was found to be 81.17 m^2/g-Pt.

4.5. References

[1] S. Sharma, B. G. Pollet, J. Power Sources 208, 96 (2012).

[2] R. Balgis, G. M. Anilkumar, S. Sago, T. Ogi, K. Okuyama, J. Power Sources 203, 26 (2012).

[3] G. M. Anilkumar, S. Nakazawa, T. Okubo, T. Yamaguchi, Electrochemistry Communications 8, 133 (2006).

[4] B. Genorio, D. Strmcnik, R. Subbaraman, D. Tripkovic, G. Karapetrov, V. R. Stamenkovic, S. Pejovnik, N. M. Markovic, Nat. Mater. 9, 998 (2010).

[5] B. Genorio, R. Subbaraman, D. Strmcnik, D. Tripkovic, V. R. Stamenkovic, N. M. Markovic, Angew. Chem. 123, 5582 (2011).

[6] W. Sheng, H. A. Gasteiger, Y. S. Horn, J. Electrochem. Soc. 157, B1529 (2010).

[7] Y. Shao, J. Liu, Y. Wang, Y. Lin, J. Mater. Chem. 19, 46 (2009).

[8] F. D. Kong, S. Zhang, G. P. Yin, N. Zhang, Z. B. Wang, C. Y. Du,

Electrochemistry Communications 14, 63 (2012).

[9] A. Masao, S. Noda, F. Takasaki, K. Ito, K. Sasaki, Electrochem. Solid State Lett. 12, B119 (2009).

[10] Z. Wang, Z. Li, H. Zhang, C. Wang, Catal. Commun. 11, 257 (2009).

[11] J. Long, W. Xue, X. Xie, Q. Gu, Y. Zhou, Y. Chi, W. Chen, Z. Ding, X. Wang, Catal. Commun. 16, 215 (2011).

[12] Z. Dong, S. J. Kennedy, Y. Wu, J. Power Sources. 196, 4886 (2011).

[13] A. B. Suryamas, M. M. Munir, T. Ogi, Khairurrijal, K. Okuyama, J. Mater. Chem. 21, 12629 (2011).

[14] M. Shao, A. Peles, K. Shoemaker, Nano Lett. 11, 3714 (2011).

[15] S. Kim, D. C. Sorescu, J. T. Yates Jr, J. Phys. Chem. C 111, 5416 (2007).

[16] J. Zhang, M. B. Vukmirovic, K. Sasaki, A. U. Nilekar, M. Mavrikakis, R. R. Adzic, J. Am. Chem. Soc. 127, 12480 (2005).

[17] K. J. J. Maryrhover, G. K. H. Wiberg, M. Arenz, J. Electrochem. Soc. 155, P1 (2008).

Chapter 5

In situ growth of Pt nanoparticles on electrospun SnO_2 fibers for anode electrocatalyst application

5.1. Introduction

Synthesis of Platinum (Pt) nanoparticles on metal-oxide matrix (Pt/MO_x) has attracted a lot of attention owing to their potential application as electrocatalyst materials [1-3]. It was assumed that interaction between Pt and metal-oxide arise the unique properties of electrocatalyst materials, particularly when the size of Pt particles scaled-down to the nanometer range. Alloying, compositing, or depositing Pt nanoparticles with metal-oxide potentially reduces the Pt-loading of electrocatalyst with reasonable electrocatalytic activity [1-3]. Thus, it opens wide opportunity for the commercialization of Pt/metal-oxide electrocatalyst.

Metal-oxide catalyst support is required to be high conductivity and high surface area. Various metal-oxides have been investigated as catalyst support materials, such as SiO_2, TiO_2, WO_3, TaO_2, SnO_2 and NbO_2, etc [2,3]. Among these oxides, SnO_2 is favorable to be applied, due to its remarkable properties such as high electron mobility, high conductivity, and corrosion resistance [4-6]. However, those distinct properties would be meaningless without high surface area. Therefore, the structural engineering to enhance surface area is indispensable for electrocatalyst application. It was proven that the structural engineering of catalyst support would enhance the catalytic properties [7].

The structural engineering of Pt/SnO_2 into fiber would enhance the overall

performance of electrocatalyst, due to the fact that fiber provides an easy access to electron transport along an alignment that is contrary to that of nanoparticles where there is a significant interface between particles that may add resistance to the system [8]. Herein, we report a facile method to synthesize Pt nanoparticles on the electrospun SnO_2 fiber matrix via a facile electrospinning method. The processing technique and the physical properties of prepared fibers are reported herein.

5.2. Experiment

The raw materials used in the experiment were polyacrylonitrile (PAN, M_W = 150000 gr/mol, Sigma Aldrich, USA), tin chloride pentahydrate ($SnCl_4 \cdot 5H_2O$, Nacalai Tesque, Japan) and hexachloroplatinic acid ($H_2PtCl_6 \cdot 6H_2O$, Mitsuwa Chemical, Japan) and *N,N*-dimethylformamide (DMF, Sigma Aldrich, USA). Three precursors were prepared for electrospinning as a function of PAN concentration. The mass of tin chloride pentahydrate, hexachloroplatinic acid, and DMF were kept constant 1, 0.05, and 12.8 g. Meanwhile, the mass of PAN was adjusted, so that the concentration of PAN were 8, 10, and 12 wt. %. The preparation of precursor was very critical and careful attention is necessary.

Each precursor was prepared by mixing three initial-precursors: P1, P2, and P3, which contained raw materials as tabulated in Table 1. Briefly, P2 was mixed to P1 and finally P3 was added to the mixture (P1+P2). All mixing procedures were done using a hot plate stirrer at 80 ^{o}C under vigorous stirring until a transparent precursor was obtained.

Table 5. 1. The composition of chemical materials used in electrospinning.

	Raw Material	Precursor		
		S1	**S2**	**S3**
1	PAN (gr)	1.2	1.54	1.89
	DMF (gr)	10.35	10.35	10.35
2	$SnCl_4.5H_2O$ (gr)	1	1	1
	DMF (gr)	2	2	2
3	$H_2PtCl_6.6H_2O$ (gr)	0.05	0.05	0.05
	DMF(gr)	0.45	0.45	0.45

The general setup for electrospinning was similar to that of our reported work [9]. The voltage, distance, flow-rate, and rotation velocity were 14 kV, 23 cm, 20 μl/min, and 450 rpm, respectively. The electrospun composite nanofibers were then calcined at 500 ^{o}C at a heating rate of 2 ^{o}C min^{-1} for 4 h under an ambient atmosphere.

The morphology of fibers was examined using a transmission electron microscope (TEM; Topcon EM-002BF) and a field emission scanning electron microscope (FE-SEM; Hitachi S-5000). The crystalline structures of fibers were then examined using X-ray diffraction (XRD) measurement (Rigaku RINT2000 X-ray diffractometer with nickel filtered Cu-Kα (λ=0.154 nm) radiation at 40 kV and 30 mA with a scanning rate of 0.02^{o}/2θ). Inductively coupled plasma measurement (ICP, SII,

S6000) was applied to determine the Pt-loading of Pt/SnO_2 fibers. A potentiostat (Hokuto Denko, HR-301) was used for cyclic voltammetry measurement. The measurement setup of cyclic voltammetry was similar to the previous work [7,10,11]. Briefly, the catalyst ink was prepared by mixing Pt/SnO_2 fibers with alcohol and water, then replaced to the glassy carbon disk (ϕ = 0.5 cm) and dried to produce a thin film catalyst layer. All measurements were performed at 25°C using an aqueous electrolyte solution of 0.1 M $HClO_4$. The electrolyte solution was saturated with nitrogen gas for 30 minutes before cyclic voltammetry (CV) measurements. The CV measurements were scanned between 0 and 1.2 V vs. RHE with a sweep rate of 100 mVs^{-1}.

5.3. Results and Discussions

Three precursors containing various amount of PAN such as 8, 10, and 12 wt. % were used to prepare samples namely S1, S2, and S3. Figure 1(a) shows the wide-angle of XRD patterns of S1, S2, and S3. Figure 1(b) is the zoomed-image of Figure 1(a) which clearly shows Pt (111) diffraction peak. It is shown that all samples were composed of pure crystalline SnO_2 and Pt. This observation confirmed that Pt nanoparticles can be grown in situ simultaneously with metal-oxide formation by calcination. Previous study reported the DMF-reduction method to synthesize metal nanoparticle [12]. However, this phenomenon was not occurred here, as confirmed by XRD spectrum of as-spun fibers (see supporting information, SI 1). The diffraction peaks of SnO_2 and Pt can be indexed to the tetragonal rutile and face-centered cubic structure respectively, according to the JCPDS Cards Nos. 41-1445 and 04-0802. The crystallite sizes of SnO_2 were calculated following the Scherer law and were 25.34 (S1), 23.9 (S2), and 29.6 (S3) nm. Meanwhile, the crystallite sizes of Pt were calculated to be

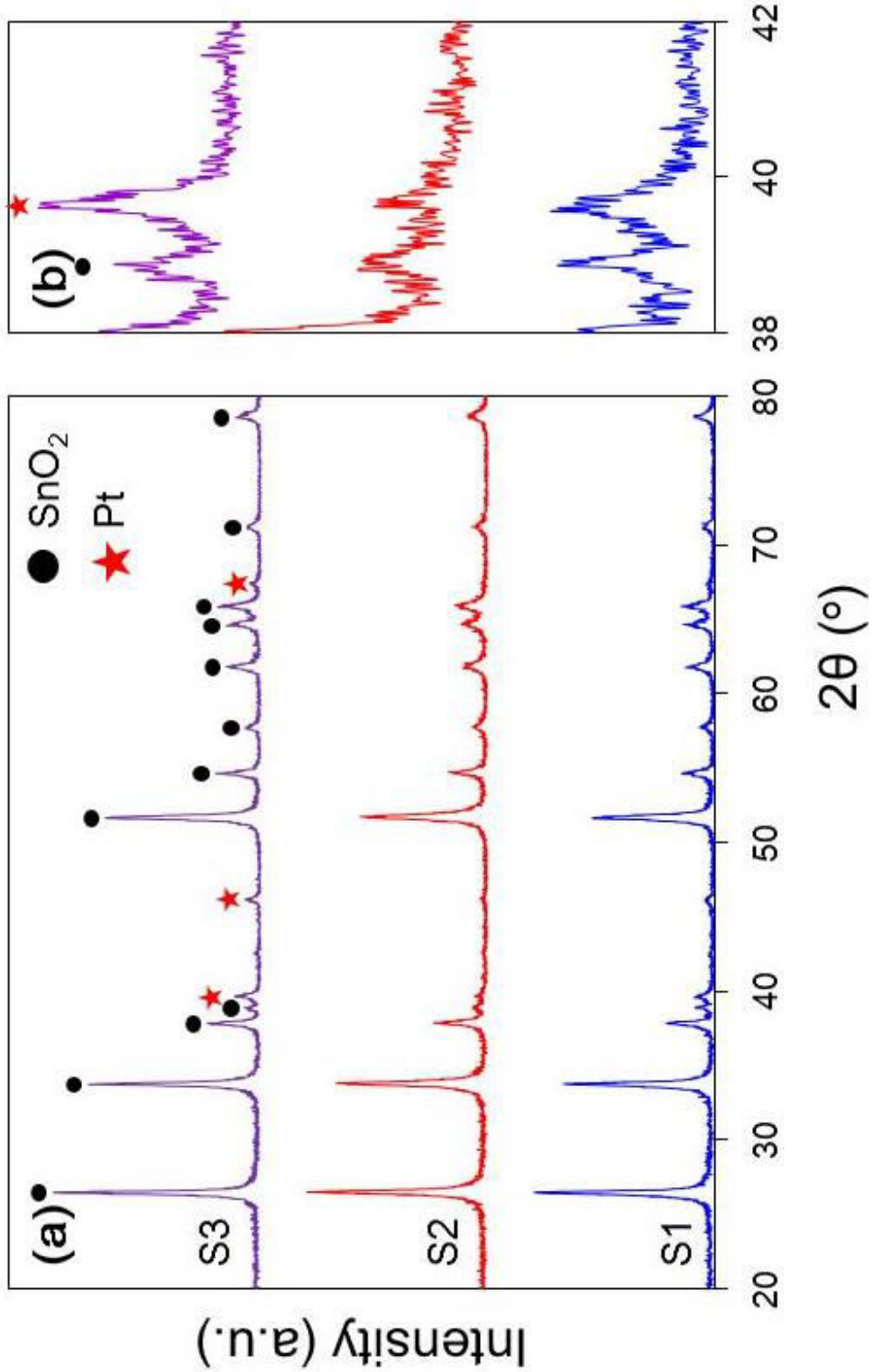

Fig. 5.1. Wide-angle XRD pattern of Pt/SnO_2 nanofibers (a) and its magnification (b).

25.24, 6.3, and 32.2 nm for S1, S2, and S3. It is interesting to note that the crystallite size of Pt particle dramatically reduced while the PAN was 10 wt. % (S2), in addition the smallest crystallite size of SnO_2 was also found on sample S2. We concluded that changes on the crystallite size of of SnO_2 and Pt were affected by PAN concentration. Presumably, the as-spun fibers contained PAN, $SnCl_4$ and H_2PtCl_6 formed clusters of $SnCl_4$/PAN and H_2PtCl_6/PAN. The presence of PAN inhibits the crystal growth SnO_2 and Pt to the bulk size so that the crystallite sizes of SnO_2 and Pt were decreased while the PAN concentration increased from 8 to 10 wt. %. However, the crystallite size of SnO_2 and Pt become larger at a polymer concentration of 12 wt. %, probably due to the excess of PAN cluster aggregated each other with PAN from other $SnCl_4$/PAN and H_2PtCl_6/PAN clusters and then rapidly evaporated during heating treatment and allowed the crystal growth to the bigger size. In addition, the transformation of PAN into carbon during calcination may play a role in Pt reduction. The optimum size of Pt particles for electrocatalytic activity was reported around 5 nm [7,10]. From this point of view, we conclude that S2 is the best to be used as an electrocatalyst.

Figure 2 shows the FE-SEM (a), TEM (b), STEM (c), and HR-TEM (d) of prepared fibers S2. The average diameter of fiber is around 1000 nm, quite bigger than the common electrospinning reports, due to the high concentration of PAN. In order to confirm the presence of Pt nanoparticles, STEM and HR-TEM images were taken and presented in Figure 2(c) and 2(d). It was confirmed by both images that Pt nanoparticles were exist on the SnO_2 fiber matrix. STEM image showed a broad range of particles size distribution. The average size of Pt nanoparticles sampled from STEM images was 6.4 nm with standard deviation 1.7 nm (see Supporting Information, SI 2). The Pt loading of this sample was determined as 4.05 wt. % by ICP measurement. Elemental

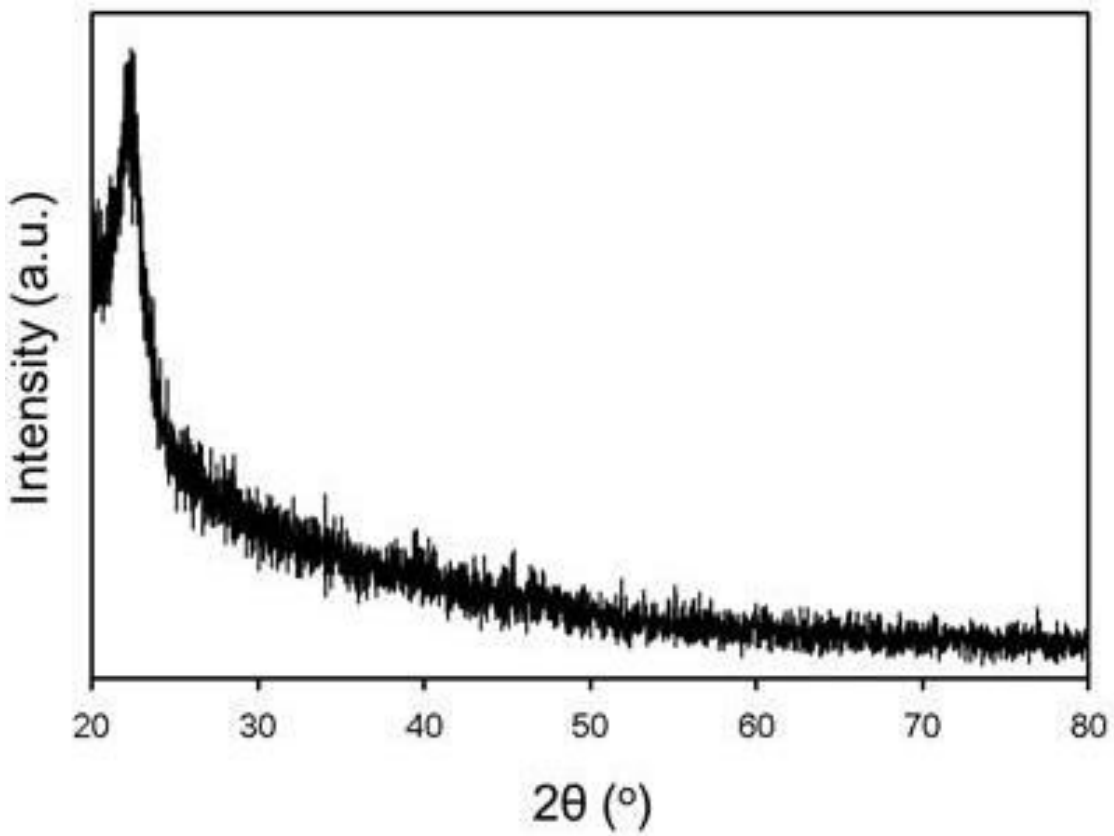

Fig. 5. SI. 1. XRD spectrum of electrospun fibers prior calcination.

mapping of sample S2 was conducted to verify the atomic distribution on the prepared nanofiber and shown in Figure 3. It is shown that Sn, O, and Pt atoms were exist in the nanofibers and well-distributed on the nanofiber matrix. Interestingly, there is no PtO formation as confirmed by XRD patterns, even though O atoms was exist in the nanofibers.

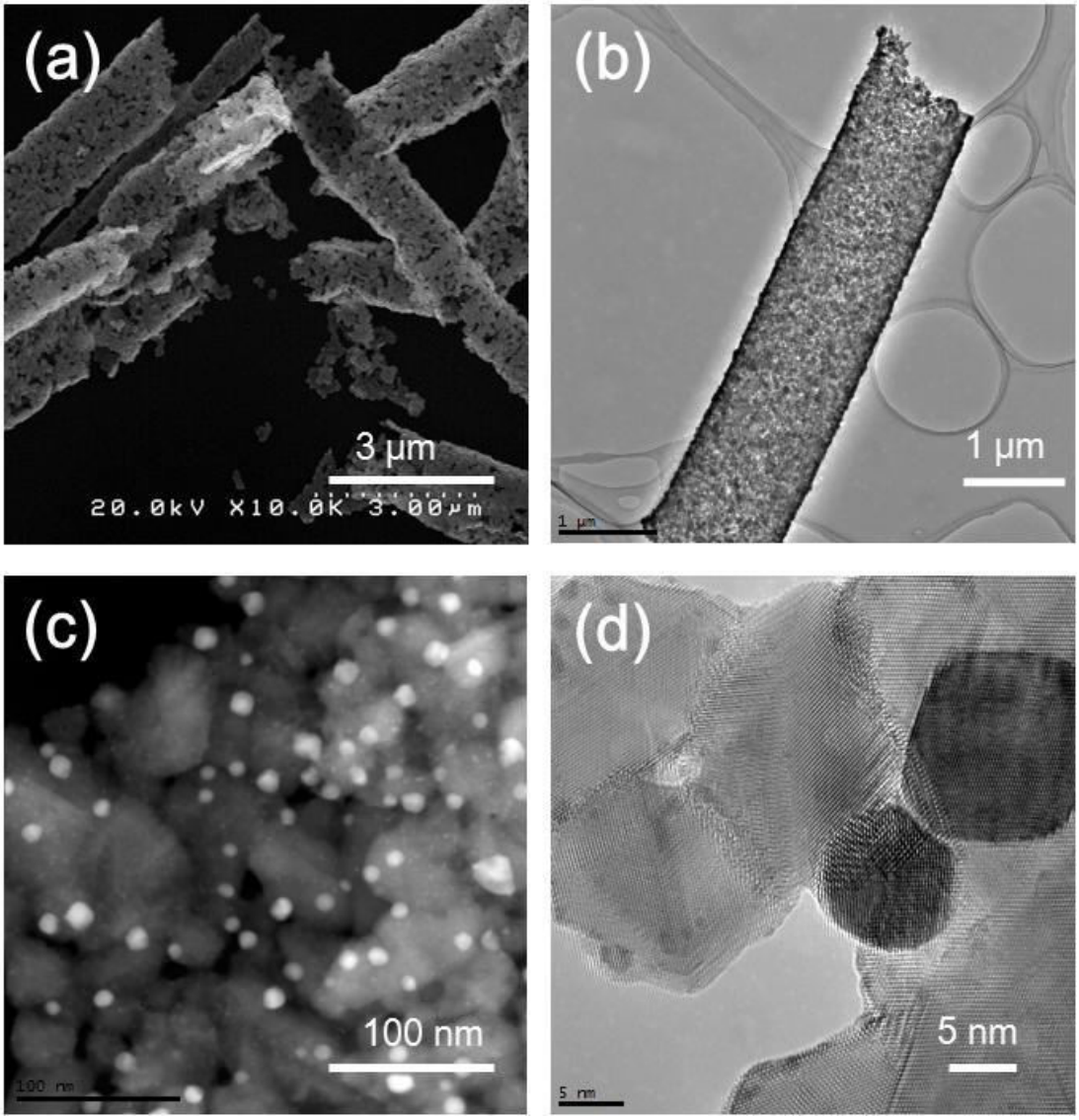

Fig. 5.2. FE-SEM (a), TEM (b), STEM (c), and HR-TEM (d) images of sample S2 Pt/SnO_2 fibers.

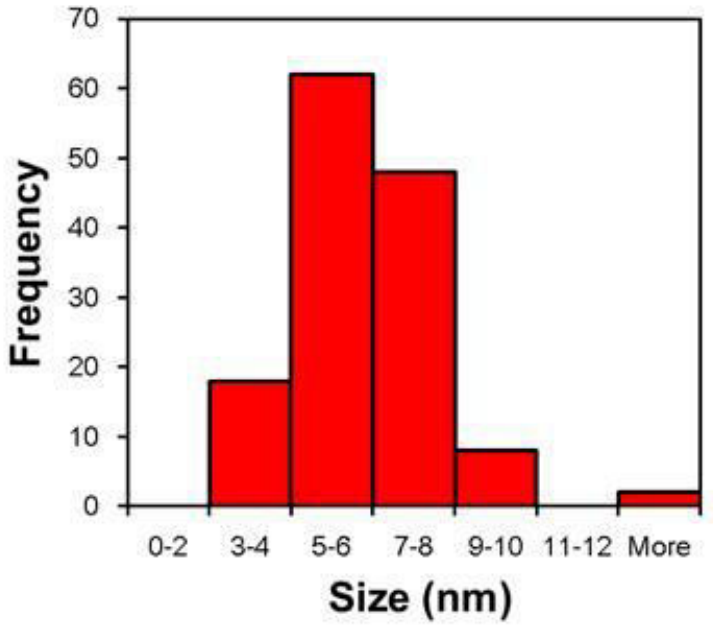

Fig. 5. SI. 2. Size distribution of Pt nanoparticles.

The electrochemical properties of prepared Pt/SnO_2 fibers and commercial Pt/C catalyst (46 wt.%, Tanaka Kikinzoku Kogyo Co., Ltd (TKK)) were measured using cyclic-voltammetry measurement. The voltammogram recorded after 200th cycles are presented in Fig. 4. As a characteristic of cyclic votalmmogram, there are three regions in a CV-curve that correspond to hydrogen adsorption-desorption ($0.06 < E < 0.4$), double-layer charging ($0.4 < E < 0.6$), and Pt oxidation-reduction activities ($E > 0.6$). However the CV-curve of Pt/SnO_2 nanofiber only allowed the hydrogen adsorption-desorption reaction without Pt oxidation-reduction. This means that the Pt/SnO_2 nanofiber only applicable to be used as an anode electrocatalyst. The detail explanation of can be found elsewhere [11]. In order to examine the feasibility of Pt/SnO_2 nanofiber to be applied as an anode electrocatalyst, the electrochemically active surface area (ECSA) was calculated. The ECSAs were calculated to be 15.9, 87.8, 20.3, and 94.8 m^2g^{-1}Pt for S1, S2, S3, and commercial electrocatalyst respectively. It is

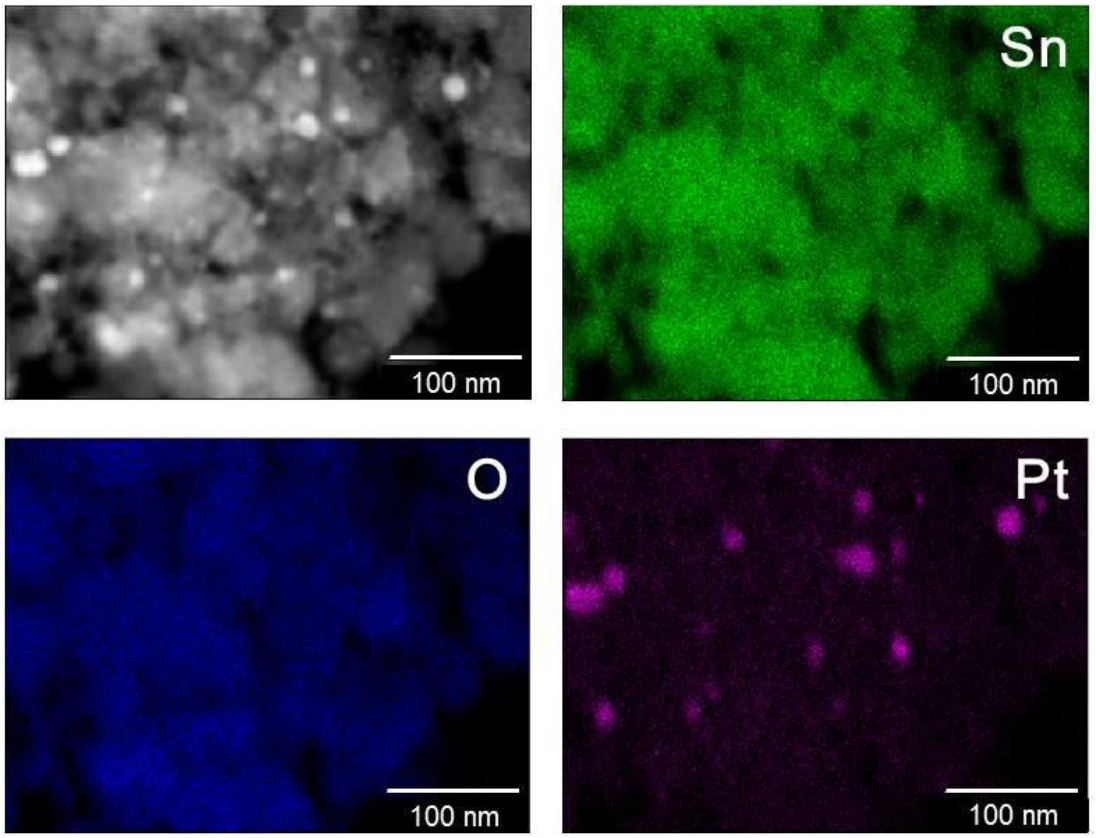

Fig. 5.3. Elemental mapping of sample S2 Pt/SnO_2 fibers.

noteworthy mention that the highest ECSA value of Pt/SnO_2 nanofibers (87.8 m^2g^{-1}Pt) is lower than the ECSA value of commercial caltayst (94.8 m^2g^{-1}Pt). However, the Pt loading on Pt/SnO_2 nanofibers (4.05 wt. %) is very much lower than that of the commercial one (46 wt. %). It offers great advantages for cost-effective industrial scale production.

5.4. Conclusions

The present study demonstrated a facile method to synthesize Pt nanoparticle on the electrospun SnO_2 fibers matrix. Pt nanoparticles were successfully grown in situ

on the electrospun SnO_2 fibers without any formation of byproduct. The size of Pt nanoparticle was span in the range of 6-32 nm by simply varying the PAN concentration in the precursor. The highest ECSA value of Pt/SnO_2 fibers was found to be 87.8 m^2g^{-1}Pt with Pt loading of 4.05 wt. %, which is very competitive to the commercial Pt/C electrocatalyst.

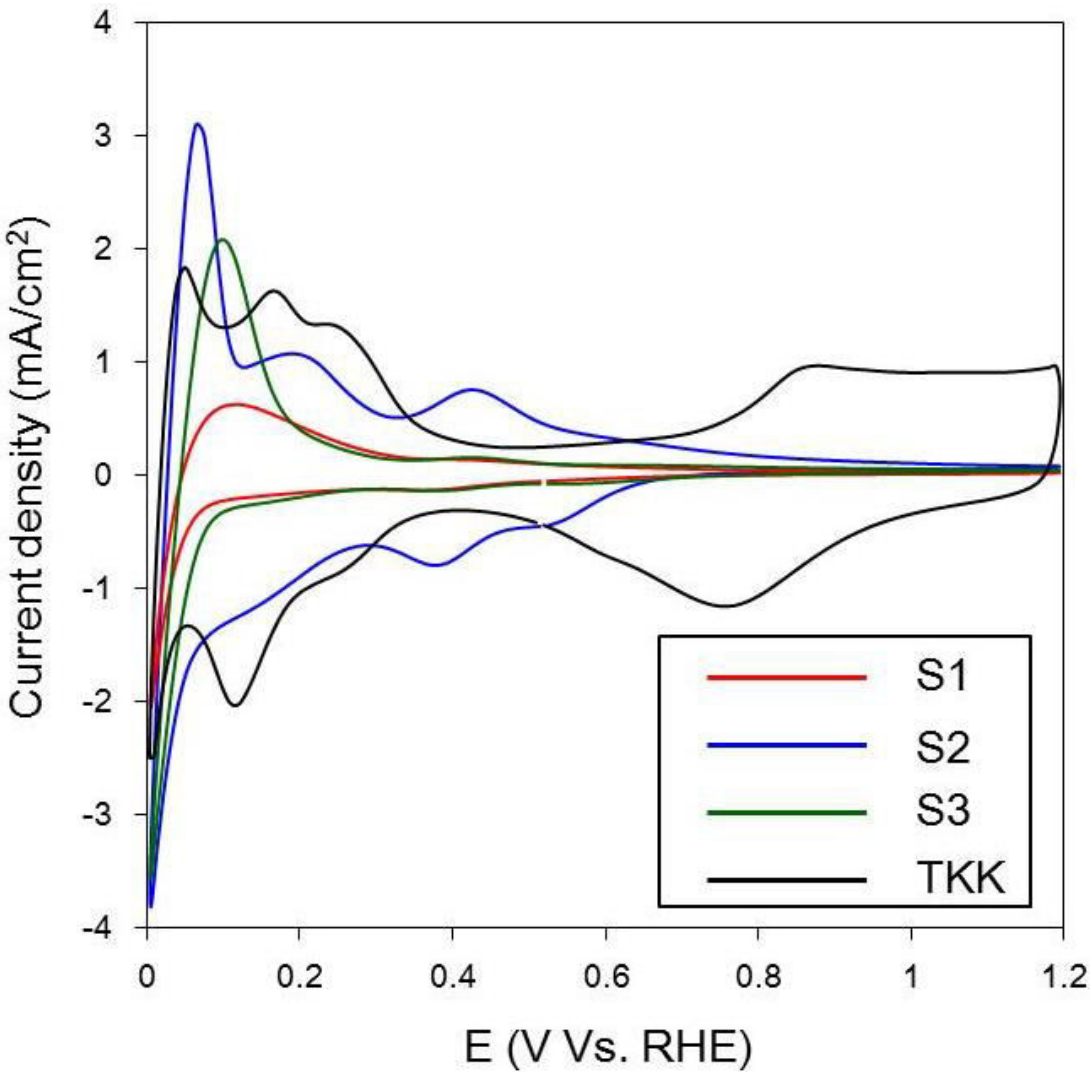

Fig. 5.4. Cyclic voltammogram of prepared Pt/SnO_2 fibers and commercial Pt/C catalyst in nitrogen-saturated 0.1M $HClO_4$ measured at100 mVs^{-1}.

5.5. References

[1]. Y.-J. Wang, D. P. Wilkinson, J. Zhang, Chem. Rev. 111, 7625 (2011).

[2]. V. Tripkovic, F. Abild-Pedersen, F. Studt, I. Cerri, T. Nagami, T. Bligaard, J. Rossmeisl, ChemCatChem. 4, 228 (2012).

[3]. N. Kamiuchi, T. Matsui, R. Kikuchi, K. Eguchi, J. Phys. Chem. C 111, 16470 (2007).

[4]. A. Masao, S. Noda, F. Takasaki, K. Ito, K. Sasaki, Electrochem. Solid State Lett. 12, B119 (2009).

[5]. P. Zhang, S. Y. Huang, B. N. Popov, J. Electrochem. Soc. 157, B1163 (2010).

[6]. F. Takasaki, S. Matsuie, Y. Takabatake, Z. Noda, A. Hayashi, Y. Shiratori, K. Ito, K. Sasaki, J. Electrochem. Soc. 158, B1270 (2011).

[7]. R. Balgis, G. M. Anilkumar, S. Sago, T. Ogi, K. Okuyama, J. Power Sources 203, 26 (2012).

[8]. Z. Dong, S. J. Kennedy, Y. Wua, J. Power Sources 196, 4886 (2011).

[9]. A. B. Suryamas, M. M. Munir, T. Ogi, C. J. Hogan Jr., K. Okuyama, Jpn. J. Appl. Phys. 49, 115003 (2010).

[10]. R. Balgis, G. M. Anilkumar, S. Sago, T. Ogi, K. Okuyama, Fuel Cells 12, 665 (2012).

[11]. A. B. Suryamas, G. M. Anilkumar, S. Sago, T. Ogi, K. Okuyama, Catal. Commun 33, 11 (2013).

[12]. H. Kawasaki, H. Yamamoto, H. Fujimori, R. Arakawa, Y. Iwasaki, M. Inada, Langmuir 26, 5926 (2010).

Chapter 6

Conclusions

The preparation of nanostructured particle and fibrous materials using spray process (i.e. spray pyrolysis and electrospray) were systematically described in this thesis. The application as catalysts especially for fuel cell are also studied, and the major conclusions obtained in the thesis are as follows:

1) This study demonstrated a facile strategy for the production of a novel electrocatalyst support material, i.e., porous carbon derived from phenolic resin using spray pyrolysis. The morphology of the phenolic resin derived carbon was controlled simply by the addition of appropriate amount of PSL template particles to the precursor. Pt deposition on the phenolic resin derived carbon was achieved using a standard industrial impregnation method. Agglomeration-free and well dispersed Pt nanoparticles of average size 3.91 nm were observed on the surfaces of the porous carbon particles. The high performance of the porous Pt/C electrocatalyst was proven by its high mass activity and electrochemically active surface area, which were 450.81 mA mg−1-Pt and 81.78 m2 g−1-Pt, respectively. The porous Pt/C mass activity value is twice those of the available commercial Pt/C catalyst.es remained in both samples. The existence of pores at moderate temperatures allows various applications for the prepared particles, such as electrodes and catalysts.

2) Artistic hollow and porous carbon particles were prepared by spray pyrolysis of a dual polymer system and were described in this study. The morphology of the prepared particles can be well tailored by precisely tuning the attractive or repulsive

force in a droplet. The as-prepared particles readily adsorb CO_2 because they contain various aromatic groups derived from the phenolic resin and large active surface areas. This study opens a new opportunity for the development of advanced adsorbent material for the future needs. The effect of various experimental conditions to the particles morphology and adsorption ability will be addressed in further investigations. Our results suggest that morphology of particles influences their adsorption and CO_2 storage ability.

3) The present study demonstrated an effective strategy to design an anode catalyst using Pt/SnO_2 nanofibers. Pt nanoparticles were successfully grown in situ on the electrospun SnO2 nanofibers. The Pt/SnO_2 nanofibers showed unique electrocatalytic activity by allowing a hydrogen oxidation reaction while simultaneously inhibits an oxygen reduction reaction. The ECSA of Pt/SnO2 nanofibers was found to be 81.17 m2/g-Pt.

4) A facile method to synthesize Pt nanoparticle on the electrospun SnO_2 fiber matrix was demonstrated in the present study. Pt nanoparticles were successfully grown in situ on the electrospun SnO_2 fibers without any formation of by product. The size of Pt nanoparticle as in the range of 6–32 nm by simply varying the PAN concentration in the precursor. The highest ECSA value of Pt/SnO_2 fibers was found to be 87.8 m^2 g^{-1}Pt with Pt loading of 4.05 wt%, which is very competitive to the commercial Pt/C electrocatalyst.

Appendix I: List of Figures

Fig. 1.1. Nanoparticle to fine structured particle for better functional applications 1

Fig. 1.2. Ceramic development for dental application 3

Fig. 1.3. TEM images of the prepared carbon nanotubes 4

Fig. 1.4. A schematic illustration of particle formation on surface of charged colloidal particles 7

Fig. 1.5. Electrospining setup 10

Fig. 1.6. Thesis outline 14

Fig. 2.1. Schematic diagram of the experimental setup 23

Fig. 2.2. TGA thermograms of the phenolic resin, phenolic resin-PSL composite, and PSL 25

Fig. 2.3. FE-SEM image of porous carbon using 4wt% P^+ and phenol resin concentration of (a) 0.1, (b) 0.25, (c) 0.5, (d) 1, and (e) 2 wt%; and (f) schematic diagram of Pt deposition phenomena on the surfaces of microporous and macroporous carbon 27

Fig. 2.4. FT-IR spectra of the PSL and phenolic resin derived carbon 28

Fig. 2.5. (a), (b) FE-SEM images of the porous Pt/C catalyst, (c), (d) TEM image of the porous Pt/C catalyst, (e) HR-TEM image of the distribution of 20 wt% Pt on the carbon surface, (f) histogram of Pt nanoparticles distribution, and (g) XRD patterns of the porous Pt/C catalyst after reheating at 120°C for 120 min under vacuum 30

Fig. 2.6. FE-SEM images of microporous Pt/C catalyst 31

Fig. 2.7. Electron tomography (ET) images of the porous Pt/C catalyst: (a) in the x, y, and z directions, (b) in the x and y directions, and (c) after the reconstruction process 32

Fig. 2.8. (a) CVs of the porous Pt/C catalyst and the commercial Pt/C catalyst over 10 cycles in oxygen-free 0.1 M $HClO_4$ (cycling between 0 and 1.2 V at 50 mV s^{-1} sweep rate), (b) comparison of the ORR polarization curve of the porous Pt/C catalyst and the commercial Pt/C catalyst at a rotation rate of 1600 rpm, (c) ORR polarization curves at different rotation rates for the porous Pt/C catalyst after 10 cycles in oxygen-saturated 0.1 M $HClO_4$ at a sweep rate of 10 mV s^{-1}, and (d) Koutecky-Levich plot of the porous Pt/C catalyst at different rotation rates and potentials 34

Fig. 2.9. (a) CVs of porous Pt/C catalyst over 10 and 10,000 cycles in oxygen free 0.1 M $HClO_4$ (cycling between 0 and 1.2 V at 50 mV s^{-1} sweep rate), (b) ORR polarization curve of the porous Pt/C catalyst over 10 and 10,000 cycles at rotation rate of 1600 rpm. 36

Scheme 1 Schematic of the experimental procedure 43

Fig. 3.1. (a) The effect of AIBA concentration on zeta potential of PSL, SEM images of carbon particles prepared (b) without a template, and prepared using a template with a zeta potential of (c) 53 mV, (d) 40 mV, (e) 22 mV, (f) 12 mV, and (g) -59 mV. TEM images of carbon particles prepared using a template with a zeta potential of (h) 53 mV and (i) -59 mV 45

Fig. 3. SI.1. (a) TEM and HR-TEM images of microporous carbon particles and (b) TGA thermogram of the phenolic resin, PSL, and phenolic resin-PSL composite 48

Fig. 3.2. Schematic diagram of nanostructured particle formation during spray pyrolysis from each precursor: (a) phenolic resin, (b) phenolic resin and positively charged PSL, and (c) phenolic resin and negatively charged PSL 49

Fig. 3.3. SEM images of (a) PSL (ζ = 53 mV) and (b) PSL (ζ = -59 mV). The insets show the obtained carbon particles. (c) model of PSL arrangement in a droplet 51

Fig. 3.SI.2. Electron tomography (ET) images of: (a) hollow and (b) porous carbon particles 53

Fig. 3.SI.3. CO_2 TPD profile of hollow and porous carbon particles 54

Fig. 3.SI.4. FT-IR spectrum of porous carbon particles 57

Fig. 4.1. XRD patterns of (a) SnO_2 nanofibers and (b) Pt/SnO_2 nanofibers 64

Fig. 4.2. (a) FE-SEM image, (b) TEM image, (c) high-resolution TEM image, and (d) elemental mapping of Pt/SnO_2 nanofibers 66

Fig. 4.3. (a) Cyclic voltammogram of SnO2 nanofibers, Pt/SnO2 nanofibers, and Pt/C TKK (b) Linear sweep voltammograms of Pt/SnO2 nanofibers, (c) Linear sweep voltammograms of Pt/C TKK, (d) Kouteky–Levich plot of Pt/SnO2 nanofibers in the diffusion potential region E = 0.05 V 67

Fig. 5.1. Wide-angle XRD pattern of Pt/SnO_2 nanofibers (a) and its magnification (b) 75

Fig. 5.SI.1 XRD spectrum of electrospun fibers prior calcination 77

Fig. 5.2. FE-SEM (a), TEM (b), STEM (c), and HR-TEM (d) images of sample S2 Pt/SnO_2 fibers 78

Fig. 5.SI.2 Size distribution of Pt nanoparticles 79

Fig. 5.3. Elemental mapping of sample S2 Pt/SnO_2 fibers 80

Fig. 5.4. Cyclic voltammogram of prepared Pt/SnO2 fibers and commercial Pt/C catalyst in nitrogen-saturated 0.1M $HClO_4$ measured at 100 mVs^{-1} 81

Appendix II: List of Tables

Table 1.1. Features and applications of particles with various morphologies 2
Table 3. SI. 1 CO_2 TPD profile of hollow and porous carbon particles 55
Table 5.1. The composition of chemical materials used in electrospining 73